JPL Publication 11-16

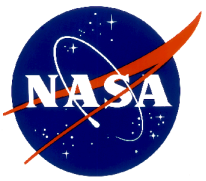

The Jovian Equatorial Heavy Ion Radiation Environment

H. B. Garrett, M. Kokorowski, and S. Kang
Jet Propulsion Laboratory, California Institute of Technology
Pasadena, California

R. W. Evans
Mori Associates
Montrose, California

C. M. S. Cohen
California Institute of Technology
Pasadena, California

National Aeronautics and
Space Administration

Jet Propulsion Laboratory
California Institute of Technology
Pasadena, California

November 2011

The research described in this publication was carried out at the Jet Propulsion Laboratory, California Institute of Technology, under a contract with the National Aeronautics and Space Administration.

ABSTRACT

From 1995 to 2003, the Galileo Heavy Ion Counter (HIC) monitored the high energy (~6 to >200 MeV/nuc), heavy ion ($_6$C to $_{28}$Ni) fluxes at Jupiter and returned data for all but 2 of the 35 orbits of the Jupiter system. HIC was based on a re-engineered Voyager Cosmic Ray System instrument and was flown in part to gain a better understanding of the heavy ion radiation environment at Jupiter than that given by the brief flyby missions of Pioneer and Voyager. These spacecraft found oxygen and sulfur to be the primary constituents in the heavy ion environment at Jupiter—HIC adds carbon, believed to be of solar origin, to the list. While the sulfur is primarily Io-genic, the oxygen is from mixed sources being either of solar origin or from sputtering off the icy moons of Jupiter. After a brief review of the instrument and its measurements, a quantitative model of the average spectra of these heavy ions in terms of radial distance and energy is presented. The data, averaged over pitch angle, are from the so-called Galileo HIC "real time event" data and cover a wide range of radial distances and local times. The model is intended to provide a reference for the background energetic carbon, oxygen, and sulfur environments near the jovian equator between ~5 and 25 R_J (the region sampled by Galileo).

KEY WORDS: Jupiter, Radiation Models, Radiation Belts, Galileo Spacecraft, Europa, High Energy Electrons, Trapped Particles, Space Radiation

Acknowledgments

The authors would like to thank Dr. I. Jun and R. Carlson for their helpful review comments. We further appreciate the help of Dr. E. C. Stone who provided the data and helped explain the operation of his HIC experiment. We particularly want to remember Dr. T. Garrard who helped us initiate this study and was a critical part of the HIC development and flight. We also extend our thanks to G. Burdick who helped provide funding for the model development and Geant4 geometric factor runs. Without his support the study would never have taken place.

EXECUTIVE SUMMARY

From 1995 to 2003, the Galileo Heavy Ion Counter (HIC) monitored the high energy (~6 to >200 MeV/nuc), heavy ion ($_6$C to $_{28}$Ni) fluxes at Jupiter and returned data for all but 2 of the 35 orbits of the Jupiter system. HIC was based on a re-engineered Voyager Cosmic Ray System instrument and was flown in part to gain a better understanding of the heavy ion radiation environment at Jupiter than that given by the brief flyby missions of Pioneer and Voyager. These spacecraft found oxygen and sulfur to be the primary constituents in the heavy ion environment at Jupiter—HIC adds carbon, believed to be of solar origin, to the list. While the sulfur is primarily Io-genic, the oxygen is from mixed sources being either of solar origin or from sputtering off the icy moons of Jupiter.

In this study, the HIC instrument and its measurements are reviewed. Based on these measurements, a quantitative model of the jovian equatorial heavy ion radiation environment was been developed. The data cover Galileo orbits C03 through J35 (excluding J5, J13, and A34). The model defines the fluxes for oxygen (5—40 MeV/nuc), carbon (5—40 MeV/nuc), and sulfur (6.3—40 MeV/nuc) between ~5–25 R_J. Average differential flux spectra for these three components are presented in terms of energy for selected radial bins. A simple fit is developed in terms of energy and radial distance that allows interpolation of the fluxes at intermediate values of the two variables. In particular, to convert the fluxes into a simple engineering model capable of interpolation, the log base 10 values were averaged over energy for selected R_J ranges and over R_J at as specific energies. These gave two flux curves, one in energy and one in radial distance. The product of these two curves at each energy and R_J were fit to a dual power law curve in energy. Assuming the two variables, energy (E) and radial distance (R), were independent, the flux at the discrete radial distances were then multiplied by the energy spectrum of the form:

$$F_j(E,R) = F_{0j}(R) \cdot E^{-A_j}\left(1+\frac{E}{E_{0j}}\right)^{-B_j}$$

Where:

F_j = Flux in units of ($n^{\#}/cm^2$ s sr MeV/nuc)
E = Energy in MeV/nuc
R = Radial value (in jovian radii, R_j) at the average of the specified interval (Table 3)
A_j, B_j = Constants to be fit
E_{0j} = Constant to be fit (in MeV/nuc)
j = subscript indicating species; carbon, oxygen, or sulfur

As the model is based on averages over pitch angle from Galileo, which primarily orbits in the jovian equatorial plane, the model is considered valid for approximately $\pm$2–3 R_J above or below that plane between 5-25 R_J. The model defaults to the ambient galactic cosmic rays (GCR) levels for carbon, oxygen, and sulfur values for fluxes below 10^{-6} $(cm^2$ s sr MeV/nuc$)^{-1}$ for carbon and oxygen and 10^{-8} $(cm^2$ s sr MeV/nuc$)^{-1}$ for sulfur. The model is intended to provide a reference for the background energetic carbon, oxygen, and sulfur environments near the jovian equator as sampled by Galileo.

TABLE OF CONTENTS

FIGURES

TABLES

THE JOVIAN EQUATORIAL HEAVY ION RADIATION ENVIRONMENT

H. B. Garrett[a], M. Kokorowski[a], S. Kang[a], R. W. Evans[b], and C. M. S. Cohen[c]

[a]*Jet Propulsion Laboratory, California Institute of Technology, 4800 Oak Grove Drive, Pasadena, California 91109*
[b]*Mori Associates, 2550 Honolulu Blvd., Montrose, California 91020*
[c]*California Institute of Technology, 4800 Oak Grove Drive, Pasadena, California 91109*

INTRODUCTION

The distribution of energetic heavy ions near Jupiter, either from cosmic rays or from trapped particles, is an important source of information about the jovian magnetospheric processes. To address a lack of knowledge of these environments the Galileo mission added an experiment, the Heavy Ion Counter (HIC), to provide detailed in-situ measurements of this environment. From 1995 to 2003, HIC monitored the high energy (~6 to >200 MeV/nuc), heavy ion ($_6$C to $_{28}$Ni) fluxes at Jupiter and returned data for all but 2 of the 35 orbits of the Jupiter system. HIC was added to gain a better understanding of the heavy ion radiation environment at Jupiter than that given by the earlier Pioneer and Voyager flybys. These spacecraft found oxygen and sulfur to be the primary constituents in the heavy ion environment at Jupiter. This study addresses the extensive Galileo HIC data set and adds carbon. The carbon is believed to be of solar origin while the oxygen is of both solar origin and from sputtering off Io and the icy moons of Jupiter (e.g., Europa and Ganymede). The sulfur is believed to be primarily Io-genic with only a small fraction of solar origin. The heavy ion model to be discussed here is intended to provide average spectra for these high energy, heavy ions as functions of energy and radial distance along the jovian equator.

GALILEO HEAVY ION COUNTER DESCRIPTION

The Galileo HIC is a modified Voyager Cosmic Ray System (CRS) instrument. HIC is composed of two solid-state detector telescopes called low energy telescopes or LETs. The two, LET B and LET E, are mounted with their central axes nearly perpendicular to the spin axis of the Galileo spacecraft, which points toward the Earth. The LETs are dE/dx versus energy sensors using a series of solid-state detector elements. LET E has thicker detectors optimized for nuclei from carbon to nickel with energies of 15–200 MeV/nuc and with a thick window that shields the detectors from low-energy protons. Lower-energy oxygen and sulfur ions are measured by the LET B that has a thinner window and a threshold of 6 MeV/nuc. The HIC geometric factors are larger than the CRS by a factor of 10, allowing much lower flux levels to be measured. Figures 1 and 2 show mass models developed for the NOVICE shielding code and the location of the LET B and LET E telescopes on Galileo. The energy channels, their designations (for LET E only), and their ranges are listed in Table 1. The geometric factors were assumed to be either 0.44 cm^2-sr (for the LETB, DUBL, and TRPL channels) or 4.0 cm^2-sr [Garrard et al., 1992]. These values are compared with Geant4 estimates in Appendix IV. A more detailed description of the HIC is given by Garrard et al. [1992].

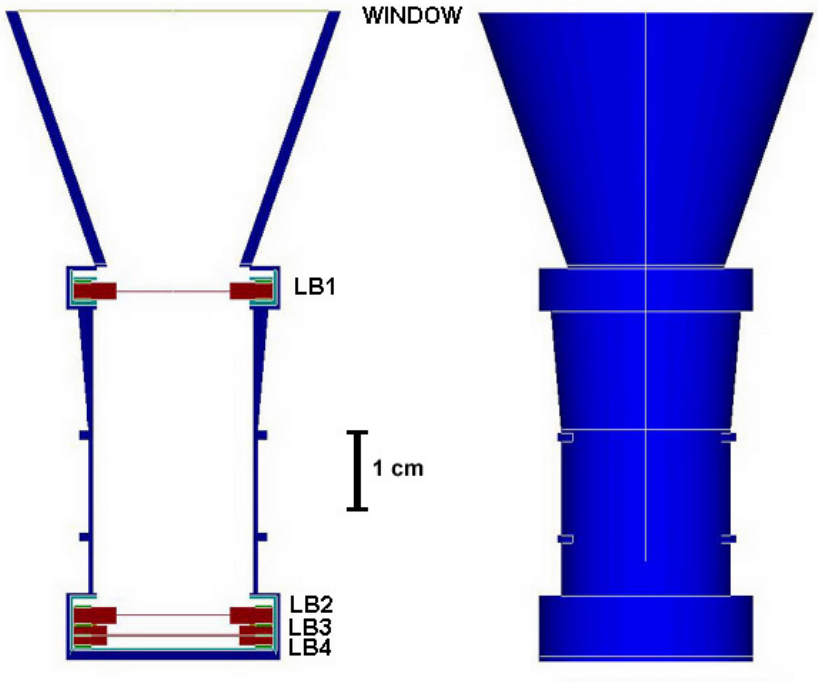

Fig. 1A. A NOVICE shielding model of the LET B telescope. Detectors LB1 through LB4 are labeled. (Bar = 1 cm)

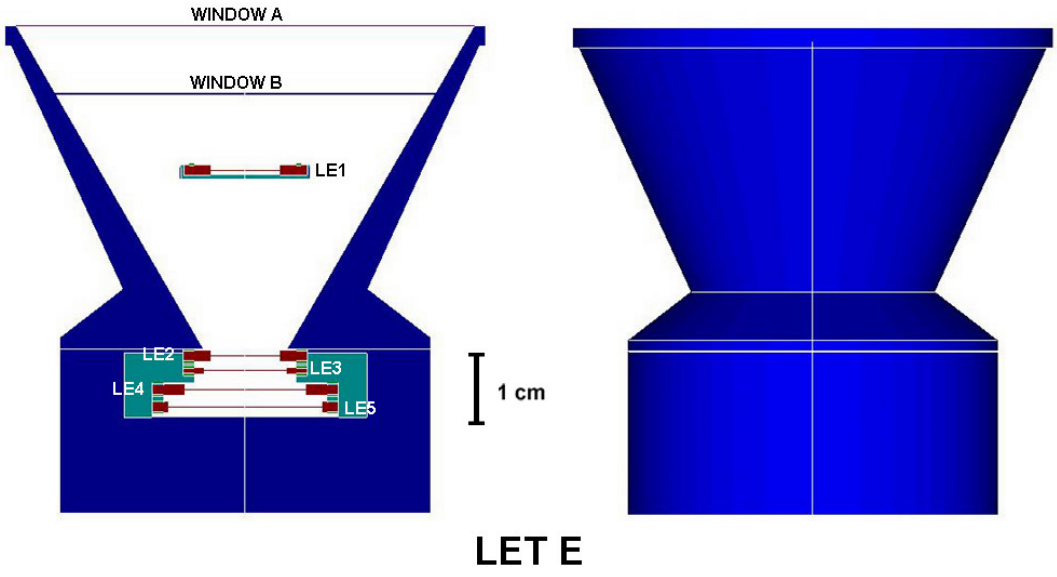

Fig. 1B. A NOVICE shielding model of the LET E telescope. Detectors LE1 through LE5 are labeled. Note that the LE1 telescope collects particles through a much smaller solid angle than the others. (Bar = 1 cm)

Table 1. Conversion matrices from measured to actual incident particle energy. The geometric center of the incident energy bin is in the last two columns. Energies are in MeV or MeV/nuc (C. M. S. Cohen, private communication).

Carbon						
	Measured		Incident		Geometric Center of Incident Energy bin MeV	Geometric Center of Incident Energy bin MeV/nuc
Channel	Low Energy MeV	Hi Energy MeV	Low Energy MeV	Hi Energy MeV		
LETB	30.000	47.275	45.600	60.000	52.307	4.359
LETB	47.275	74.498	60.000	84.000	70.993	5.916
LETB	74.498	117.398	84.000	124.800	102.387	8.532
LETB	117.398	185.000	124.800	190.800	154.311	12.859
DUBL	30.000	51.000	150.000	172.800	160.997	13.416
TRPL	62.000	88.034	164.400	177.600	170.873	14.239
TRPL	88.034	125.000	177.600	206.400	191.459	15.955
WDSTP	230.000	306.632	284.400	352.800	316.759	26.397
WDSTP	306.632	408.796	352.800	446.400	396.850	33.071
WDSTP	408.796	545.000	446.400	620.400	526.257	43.855

Oxygen						
	Measured		Incident		Geometric Center of Incident Energy bin MeV	Geometric Center of Incident Energy bin MeV/nuc
Channel	Low Energy MeV	Hi Energy MeV	Low Energy MeV	Hi Energy MeV		
LETB	45.000	72.005	68.800	91.200	79.212	4.951
LETB	72.005	115.217	91.200	131.200	109.387	6.837
LETB	115.217	184.361	131.200	195.200	160.032	10.002
LETB	184.361	295.000	195.200	296.000	240.373	15.023
DUBL	45.000	78.000	233.600	262.400	247.582	15.474
TRPL	90.000	164.864	252.800	294.400	272.808	17.051
TRPL	164.864	302.000	294.400	438.400	359.256	22.454
WDSTP	320.000	443.173	412.800	518.400	462.596	28.912
WDSTP	443.173	613.756	518.400	672.000	590.224	36.889
WDSTP	613.756	850.000	672.000	944.000	796.472	49.780

Sulfur						
	Measured		Incident		Geometric Center of Incident Energy bin MeV	Geometric Center of Incident Energy bin MeV/nuc
Channel	Low Energy MeV	Hi Energy MeV	Low Energy MeV	Hi Energy MeV		
LETB	110.000	181.203	179.200	240.000	207.384	6.481
LETB	181.203	298.496	240.000	345.600	288.000	9.000
LETB	298.496	491.713	345.600	524.800	425.877	13.309
LETB	491.713	810.000	524.800	835.200	662.052	20.689
DUBL	100.000	200.000	656.000	736.000	694.850	21.714
TRPL	212.000	428.229	704.000	825.600	762.379	23.824
TRPL	428.229	865.000	825.600	1203.200	996.675	31.146
WDSTP	800.000	1170.390	1126.400	1414.400	1262.212	39.444
WDSTP	1170.390	1712.260	1414.400	1897.600	1638.281	51.196
WDSTP	1712.260	2505.000	1897.600	2720.000	2271.887	70.996

DATA

The HIC observations were typically divided into two formats: real time and record mode. Because of the problems with the Galileo high gain antenna deployment, the HIC data return from Galileo was very limited compared with the original plans. This resulted in the real time data used for this study being averaged in time (and thus pitch angle) over tens of minutes. The data, however, were relayed to the ground as they were acquired and provide fairly complete spatial coverage from 2.8 R_J to well past 100 R_J for the Galileo orbits C03 through A34. Record mode (also called "playback") data were in a different, high time resolution format and stored on the spacecraft tape recorder for later transmission to the ground. The playback data are not used here as they are typically limited spatially to the immediate vicinity of the jovian moons and not necessarily indicative of the average environment. Further, orbit J05 and orbit J13 produced no HIC data. As the ability of the HIC and Galileo to accumulate real time data was being developed and tested during orbits G01 and G02, those data were not in a compatible form for use here. Finally, HIC shared a communication bus with the Galileo UV instrument and was not always sending data.

Fig. 2. Position of the HIC detectors on the Galileo spacecraft.

Due to the low telemetry rate, it was not possible to communicate the total number of counts as a function of species for the real time event data. Rather, representative Pulse Height Analyzed (PHA) events (e.g., "event data") were returned along with a normalization factor to account for the PHA events not returned. The HIC real time event data are returned in 'bundles' that are typically 10, 25, or 50 minutes long. Each bundle contains ~60 to ~90 representative PHA events, all with the same time marker called a unique time tag (UTT). PHA events were chronologically placed into separate telemetry buffers (one buffer for each of the following event types: LETB, DUBL, TRPL, WDSTP, and WDPEN—see Table 1) until the buffers became full. Thus, events observed during the later portions of the 'time bundle' may not be placed into the telemetry stream. To account for PHA events that are not telemetered, a separate normalization parameter called the 'livetime' was constructed using the count rate measurement. The HIC normalization (or 'livetime') is simply the number of PHA events telemetered divided by the count rate for each event type. There is a separate livetime for each time bundle and event buffer. That is:

$$Livetime_b = (PHA\ events\ returned_b)/(count\ rate_b) \quad (1)$$

Where:

count rate = the measured count rate during the given time interval

PHA events returned = refers to the number of similar ion event types telemetered via that buffer. Each PHA event type has a corresponding energy and ion species associated with it.

b = the separate event types corresponding to separate event telemetry buffers

The HIC flux is then estimated for a given PHA event type reported on the ground during a given time bundle by:

$$f(E, Species_i)_{PHA} = \sum_{j=1}^{N} \frac{1}{Livetime_{PHA} \cdot gf_{PHA} \cdot dE_{PHA}} \quad (2)$$

Where:

f_{PHA} = differential flux for species, i (i = carbon, oxygen, sulfur), and energy, E, for a given PHA event type; particles/cm^2-s-sr-MeV

E = energy of PHA event type as reported for each observation; MeV

dE = differential energy interval for energy E; MeV

$Species_i$ = carbon, oxygen, or sulfur

gf_{PHA} = geometric factor for detector channel (e.g., PHA type); cm^2-sr

j = index where the sum is over N similar PHA event types (species and energy) within the given time bundle.

The energy deposited, the approximate Z (number of protons in the nucleus) of the ion, and an uncertainty factor dZ were also returned. To correct for the outer blocking foils on the detectors, the total energy reported by the HIC (the sum of the energies deposited in each detector or measured energy) is converted to the physical incident energy by the use of a conversion matrix (Table 1). Since the matrix elements are discrete in energy, these intervals make convenient energy ranges for binning the particles in energy space. The conversion matrix from measured to actual incident energy bins and the geometric center, $\sqrt{E_{low} \cdot E_{high}}$, of the incident energy bins are listed in Table 1 for each species (C. M. S. Cohen, private communication).

If there were no telemetered events for a given species/energy bin during a time bundle and the HIC was observing, then the flux in that species/energy bin was taken to be zero. Since only a subset of the observed ion events was actually telemetered, the physical flux in that species/energy bin may well have been non-zero. However, due to the reduced telemetry rate and the use of a normalization factor, the calculated flux values are quantized into values inversely proportional to the livetime (e.g., $f \propto n / livetime$, where n = 0, 1, 2, …). By averaging over multiple time bundles at the same radial distance, the estimated flux at quantized values is assumed to approach the observed (or actual) flux.

When the average flux for a given energy interval and species is to be determined (either over a time interval or a spatial coordinate), the fluxes for the individual UTT events are summed

and then divided by the number of relevant UTTs. The raw HIC data set contained more than 1,000,000 individual PHA particle measurements at ~16,000 UTTs. This gave upwards of ~2,000 non-zero flux estimates inside an R_J of 50 for oxygen, ~1,300 for carbon, and ~180 for sulfur (see the Appendices I, II, and III for the actual number of values and non-zero values considered). The individual UTT fluxes are plotted in Figure 3 for carbon, oxygen, and sulfur as functions of R_J. Note that, on the log plots, zero values are not plotted.

AN AVERAGE MODEL IN R_J

Orbits C03 through J35 (excluding J5, J13, and A34) were considered in developing our model of the background carbon, oxygen, and sulfur ion environments along the jovian equator in terms of R_J. The fluxes (for a given species and energy range) at each UTT were averaged over selected R_J intervals between ~5-25 R_J in terms of (zero values were included):

$$f(E,R_j,k) = \sum_i \frac{1}{UTT_{R_j}} \cdot \frac{1}{Livetime_i \cdot gf_i \cdot dE_i} \qquad (3)$$

f = flux at a given E, L, and species k; units are 1/(cm^2 sr s MeV/nuc)
UTT_{RJ} = number of unique time tags for that R_J bin
gf_i = the geometric factor for i^{th} event type; units are (cm^2 sr)
$livetime_i$ = the rate normalization factor for the i^{th} PHA event type k; units are (s)
$dE_i = E_{high} - E_{low}$ for the incident energy bin; units are (MeV)

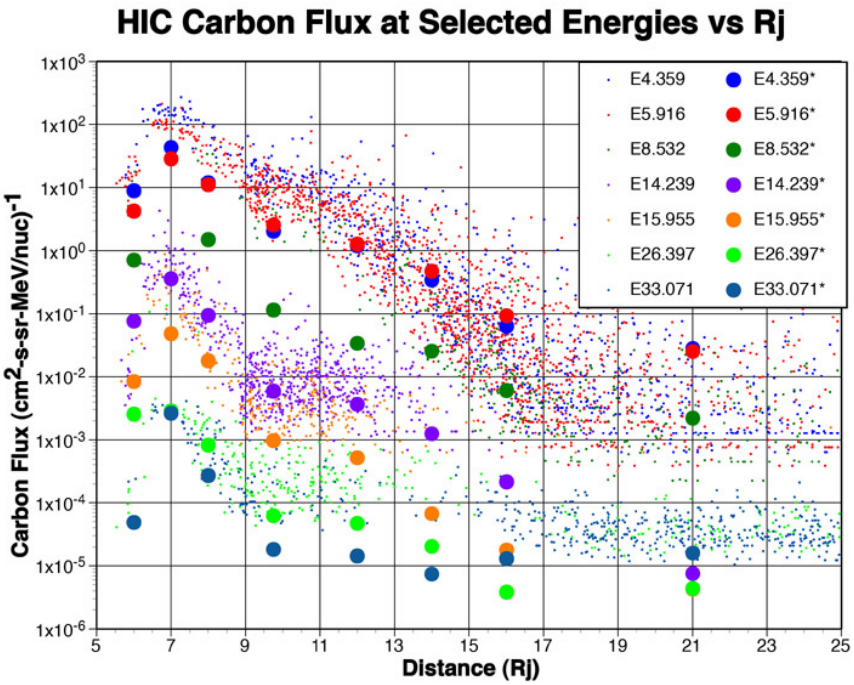

Fig. 3A. HIC carbon fluxes at selected energies (designated by "E4.359", etc.) in units of MeV/nuc versus radial distance (small symbols). Also plotted are the average values for the radial intervals and energies tabulated in Table 2 (large symbols; designated by "E4.359*", etc.).

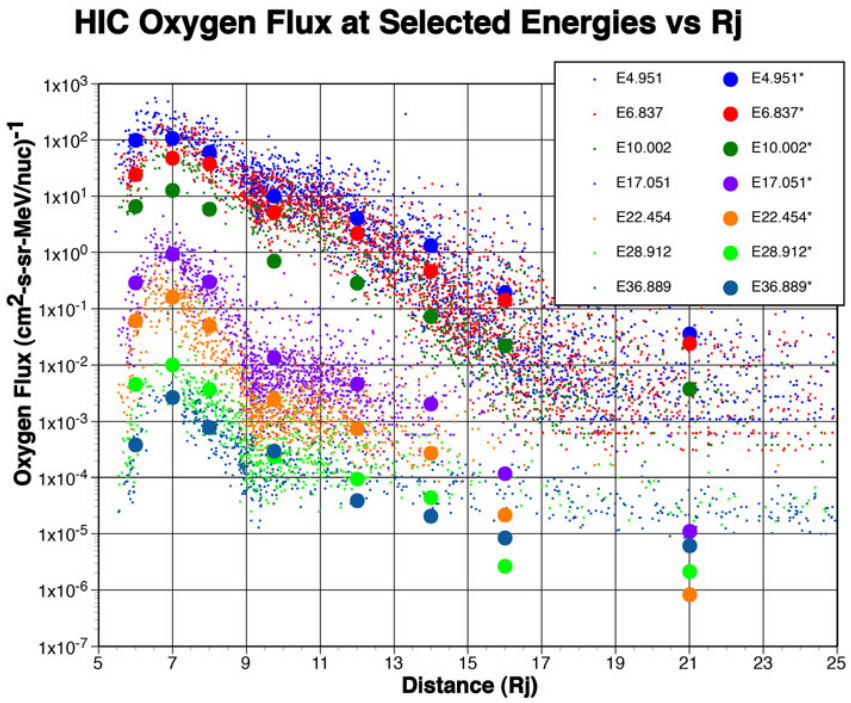

Fig. 3B. HIC oxygen fluxes at selected energies versus radial distance. Also plotted are the average values for the radial intervals tabulated in Table 2.

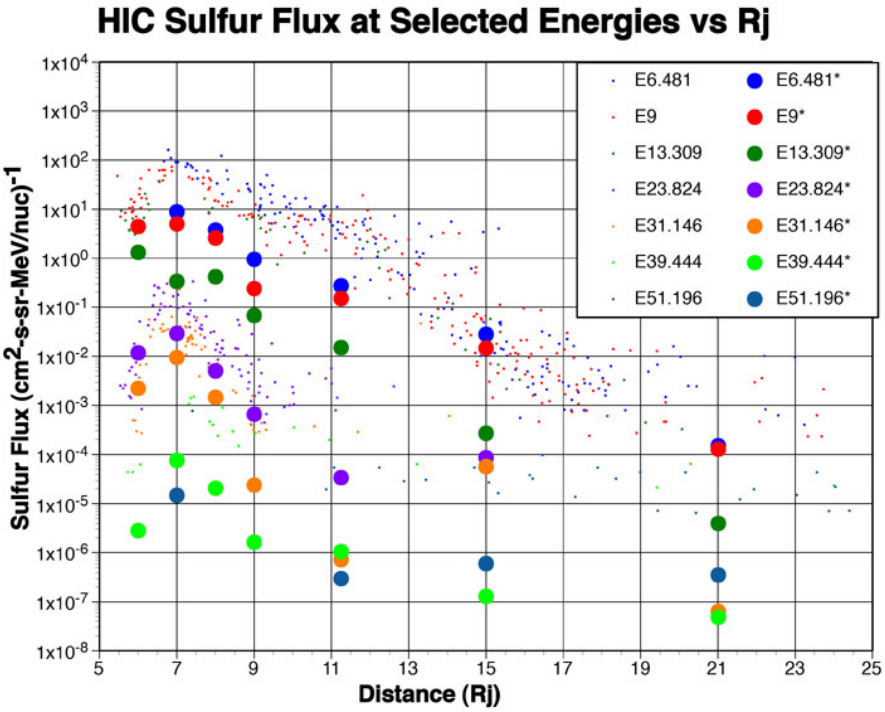

Fig. 3C. HIC sulfur fluxes at selected energies versus radial distance. Also plotted are the average values for the radial intervals tabulated in Table 2.

Table 2. Baseline HIC fluxes (n#/(cm^2-s-sr-MeV/nuc)) for carbon, oxygen, and sulfur. The energies correspond to the geometric center of incident energy bin in MeV/nuc as listed in Table 1. Blank entries correspond to fluxes for which the number of non-zero points was ≤5 and were ignored for statistical reasons. See text for discussion of why some energy channels were dropped.

Carbon

Energy (MeV/nuc)	R5.5-6.5	R6.5-7.5	R7.5-8.5	R8.5-11.	R11.-13.	R13.-17.	R17.-25.
4.359	8.94E+00	4.33E+01	1.19E+01	2.04E+00	1.20E+00	2.10E-01	2.81E-02
5.916	4.24E+00	2.85E+01	1.11E+01	2.56E+00	1.27E+00	2.92E-01	2.53E-02
8.532				1.15E-01	3.40E-02	1.62E-02	2.20E-03
14.239	7.65E-02	3.60E-01	9.43E-02	5.89E-03	3.67E-03	7.23E-04	7.58E-06
15.955		4.81E-02	1.79E-02	9.64E-04	5.17E-04	4.24E-05	
26.397	2.55E-03	2.87E-03	8.18E-04	6.24E-05	4.76E-05	1.08E-05	4.38E-06
33.071			2.72E-04	1.82E-05	1.44E-05	1.07E-05	

Oxygen

Energy (MeV/nuc)	R5.5-6.5	R6.5-7.5	R7.5-8.5	R8.5-11.	R11.-13.	R13.-15.	R15.-17.	R17.-25.
4.951	9.87E+01	1.06E+02	6.08E+01	1.01E+01	4.12E+00	1.32E+00	1.91E-01	3.55E-02
6.837	2.42E+01	4.74E+01	3.76E+01	5.17E+00	2.16E+00	4.63E-01	1.42E-01	2.41E-02
10.002	6.61E+00	1.27E+01	5.88E+00	6.98E-01	2.85E-01	7.24E-02	2.20E-02	3.73E-03
17.051	2.86E-01	9.27E-01	2.96E-01	1.34E-02	4.60E-03	2.03E-03	1.17E-04	1.10E-05
22.454	6.08E-02	1.60E-01	4.98E-02	2.45E-03	7.41E-04	2.73E-04	2.14E-05	8.31E-07
28.912	4.52E-03	1.00E-02	3.68E-03	2.34E-04	9.46E-05	4.35E-05	2.64E-06	2.11E-06
36.889	3.82E-04	2.66E-03	7.79E-04	2.95E-04	3.88E-05	2.05E-05	8.40E-06	6.14E-06

Sulfur

Energy (MeV/nuc)	R5.5-6.5	R6.5-7.5	R7.5-8.5	R8.5-9.5	R9.5-13.	R13.-17.	R17.-25.
6.481		8.84E+00	3.75E+00	9.51E-01	2.76E-01	2.80E-02	1.50E-04
9	4.42E+00	4.99E+00	2.57E+00	2.42E-01	1.50E-01	1.46E-02	1.28E-04
13.309	1.31E+00		4.20E-01	6.88E-02	1.51E-02	2.71E-04	
23.824	1.18E-02	2.93E-02	5.03E-03	6.62E-04	3.41E-05		
31.146	2.23E-03	9.53E-03	1.45E-03	2.37E-05			
39.444			2.06E-05				

The averages (see Table 2 and Fig. 3) represent a "model" for the jovian heavy ion environment at discrete energies and radial positions. To allow interpolation to intermediate distances and energies, a simple analytic model was fit to the average values. As a first step in developing the model, the average data were scrubbed prior to fitting. The number of UTT values in the R_J interval was used as the primary factor—5 non-zero values or less in a bin led to that average being dropped. Table 2 lists the average fluxes in terms of energy and R_J intervals (Tables I, II, and III in the Appendices list the number of UTT intervals included in the average (N), the number of non-zero UTT intervals (N_0) corresponding to the interval, and an estimate of the error, $\sigma = Avg/N_0^{1/2}$ for each interval). The averages from Table 2 are plotted in Fig. 3. Note that the average values plotted in Fig. 3 appear to deviate from the clustered data in the plots. The reason for this is, as has been noted earlier, the inclusion of the "zero" PHA values in the

data set and the method of plotting the data in Fig. 3 (i.e., using a logarithmic scale that suppresses very low or zero values). The highest LET B and lowest LET E channels were determined to give spurious values (the detailed geometry and the channel logic were modeled using the Geant4 code to address these issues—see Appendix IV), and it was decided to eliminate them from the two tables. The highest energy WDSTP (and the second highest WDSTP for sulfur) and the WDPEN channels were found to have too few non-zero counts for the fluxes to be meaningful and were eliminated from the fitting process.

The scrubbed data sets given in Table 2 provide flux spectra for each R interval. To convert these into a simple engineering model capable of interpolation, the log base 10 values were averaged over energy for each R range and over R at a given energy (equivalently, the geometric mean was assumed for each interval). These gave two flux curves, one in energy and one in radial distance. The product of these two curves at each energy and R were fit to a dual power law curve in energy (see Eq. 4). Assuming the two variables, E and R, were independent (note: this assumption is weak but, given the paucity of non-zero points, it was necessary to construct a statistically meaningful model), the flux at the discrete radial distances given in Table 2 multiplied by the energy spectrum given in Eq. 4 form the basis of the HIC engineering model. The corresponding values for each (E,R) interval are listed in Table 3.

The equation assumed for each species (a dual power law in energy) was:

$$F_j(E,R) = F_{0j}(R) \cdot E^{-A_j}\left(1+\frac{E}{E_{0j}}\right)^{-B_j} \qquad (4)$$

Where:

F_j = flux in units of ($n^{\#}/cm^2$ s sr MeV/nuc)
E = energy in MeV/nuc
R = radial value (in jovian radii, R_J) at the average of the specified interval (Table 3)
A_j, B_j = constants to be fit
E_{0j} = constant to be fit (in MeV/nuc)
j = subscript indicating species; carbon, oxygen, or sulfur

Table 3. Fits to the HIC data for the indicated radial distances. The constants correspond to those in Eq. 4. (Note "R^2" here refers to the regression coefficient for each fit, not radial distance.)

Carbon

A	**B**	**E_0**	**R^2**				
5.52566	0.00894115	0.92756	0.9476				
Radius	6	7	8	9.75	12	15	21
F_0	230955	450115	48497	7068.14	3969.56	985.138	457.0051
Energy	4.359	5.916	8.532	14.239	15.955	26.397	33.071

Oxygen

A	**B**	**E_0**	**R^2**					
-10.2806	18.2221	1.55683	0.97463					
Radius	6	7	8	9.75	12	14	16	21
F_0	1749081	4287791	1795300	189749	61673	21854	3212.96	632.823
Energy	4.951	6.837	10.002	17.051	22.454	28.912	36.889	

Sulfur

A	**B**	**E_0**	**R^2**				
-20.9041193	38.70714854	6.44416	0.8818				
Radius	6	7	8	9	11.25	15	21
F_0	1.96042E-05	8.7001E-05	3.19029E-06	9.56586E-07	9.65935E-07	2.75922E-07	2.25412E-09
Energy	6.481	9	13.309	23.824	31.146	39.444	51.196

To obtain intermediate values in R, the model assumes linearly interpolation between the logs of the fluxes at the R values given in Table 3. The model assumes cut-offs at flux levels corresponding to the background galactic cosmic rays (GCR) (see Fig. 7 below):

Carbon: 1e-6 (1/cm^2 s sr MeV/nuc)
Oxygen: 1e-6 (1/cm^2 s sr MeV/nuc)
Sulfur: 1e-8 (1/cm^2 s sr MeV/nuc)

These interplanetary background GCR flux levels (Fig. 7) are assumed when the model fit predicts a lower value. The energy ranges for each species are:

Carbon: 5–40 MeV/nuc
Oxygen: 5–40 MeV/nuc
Sulfur: 6.3–40 MeV/nuc

Following are plots of the model fits compared with the actual average values for carbon, oxygen, and sulfur based on the model as defined in Table 3.

The model results plotted in terms of E and R are presented in Figs. 4, 5, and 6 are for the Galileo data without consideration of the effects of magnetic latitude. The Galileo orbit, however, is typically near the jovian equatorial plane.

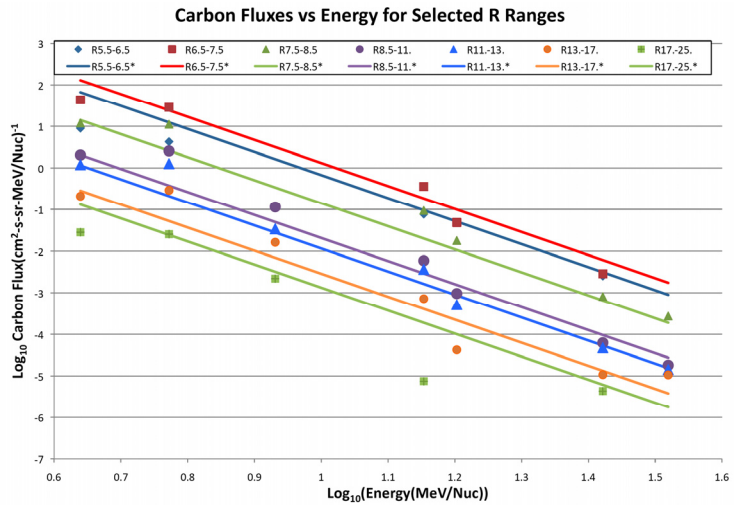

4A.

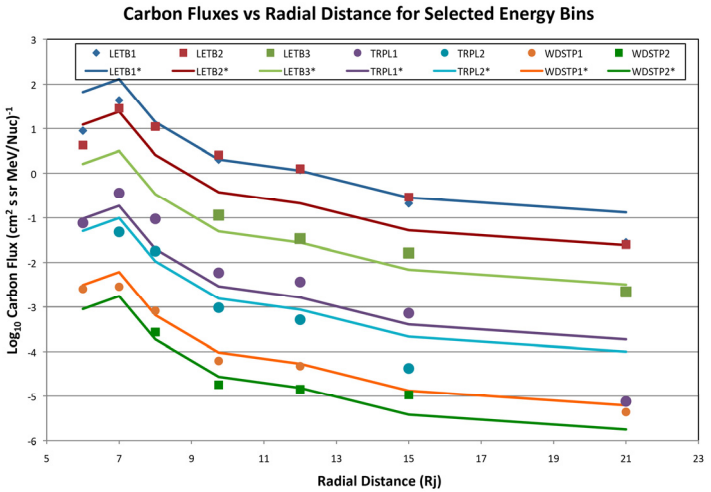

4B.

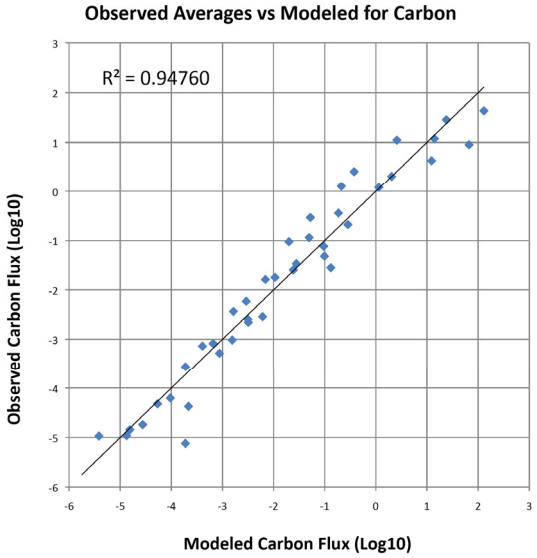

4C.

Fig. 4. HIC average observations (points) compared to the fits to the carbon data. Flux units are (1/cm^2 s sr MeV/nuc). The regression is for the log$_{10}$ of the flux values. (Estimates of the errors in the average values are provided in the appendices.)

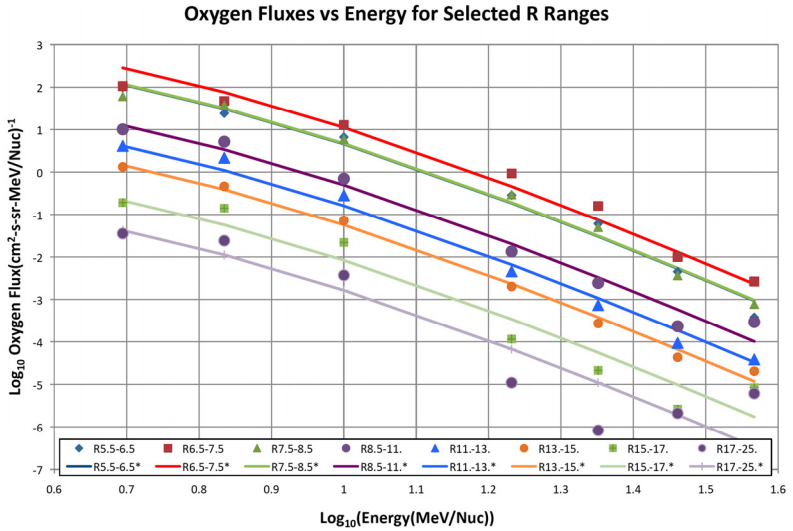

5A.

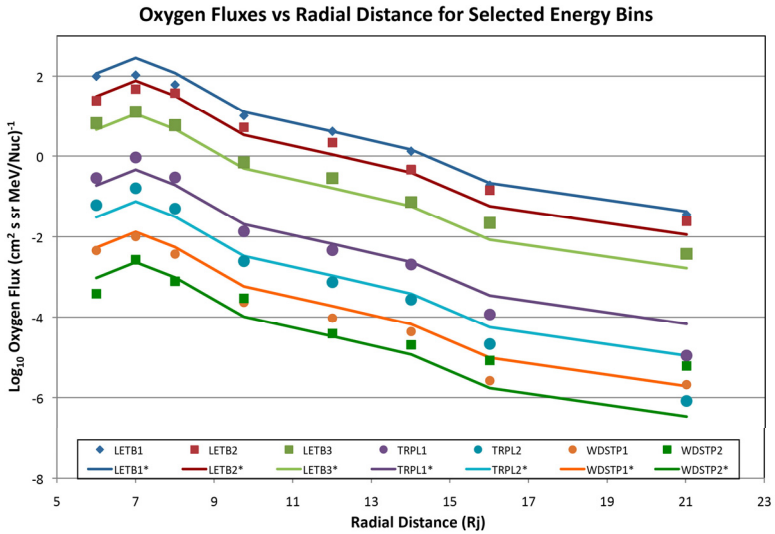

5B.

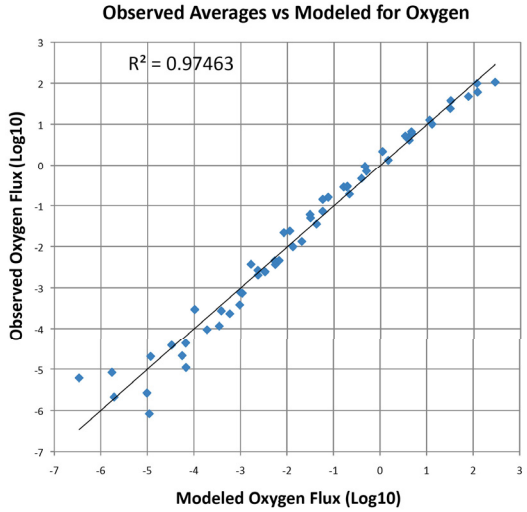

5C.

Fig. 5. HIC average observations (points) compared to the fits to the oxygen data. Flux units are (1/cm^2 s sr MeV/nuc). The regression is for the log$_{10}$ of the flux values. (Estimates of the errors in the average values are provided in the appendices.)

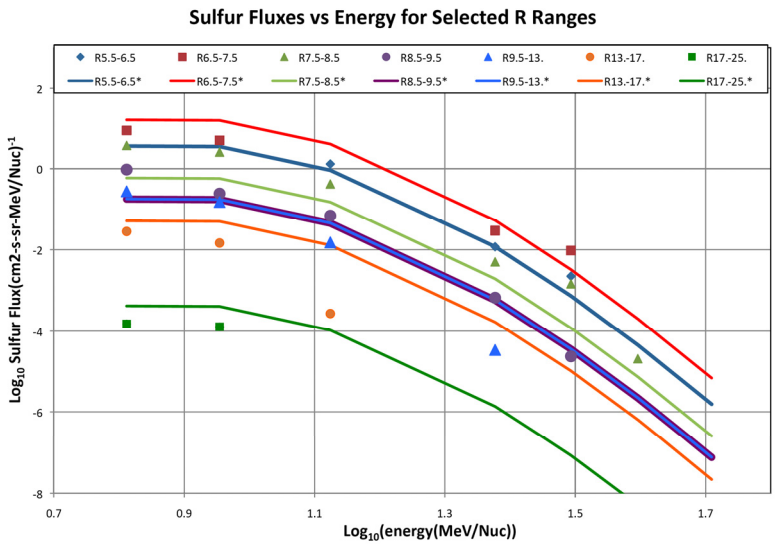

6A.

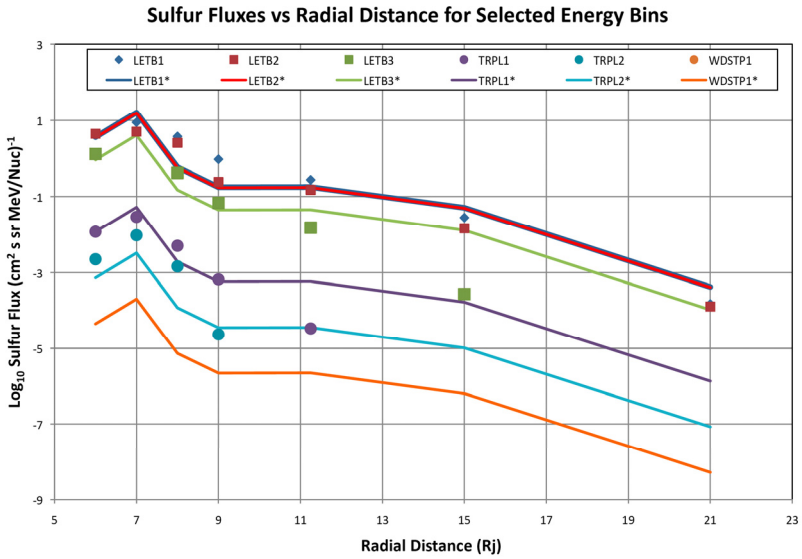

6B.

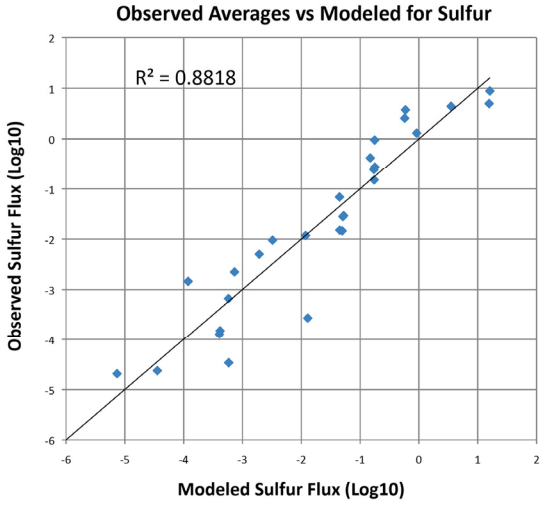

6C.

Fig. 6. HIC average observations (points) compared to the fits to the sulfur data. Flux units are (1/cm^2 s sr MeV/nuc). The regression is for the log$_{10}$ of the flux values. (Estimates of the errors in the average values are provided in the appendices.)

Cohen et al. (2001) in earlier work have noted that there is a variation in the HIC flux as a function of distance from the magnetic equatorial plane (e.g., due to pitch angle variations with magnetic latitude) for individual orbits. In this study, we estimated this effect by taking ratios of the particle fluxes off the magnetic equatorial plane regions to the ratios of the fluxes near the magnetic equator. In particular, the ratios of the fluxes for locations with maximum mirror pitch angles less than 60° (e.g., off the magnetic equator) divided by those with maximum mirror pitch angles between 60° to 90° (near the magnetic equator) were compared. These results showed that there was no observable latitude effect within ~10 R_J (most likely because Galileo was normally near the magnetic equator in this region). The ratio averaged ~80% in the region of 10–20 R_J (that is the off-axis fluxes were about 80% of the equatorial values). These variations are well within the uncertainties of our models and are therefore not considered important for this study. Outside ~20 R_J we found the ratios much more variable with the off-equatorial values higher on the average (we attribute this to uncertainties in the magnetic field model, VIP4, that we used).

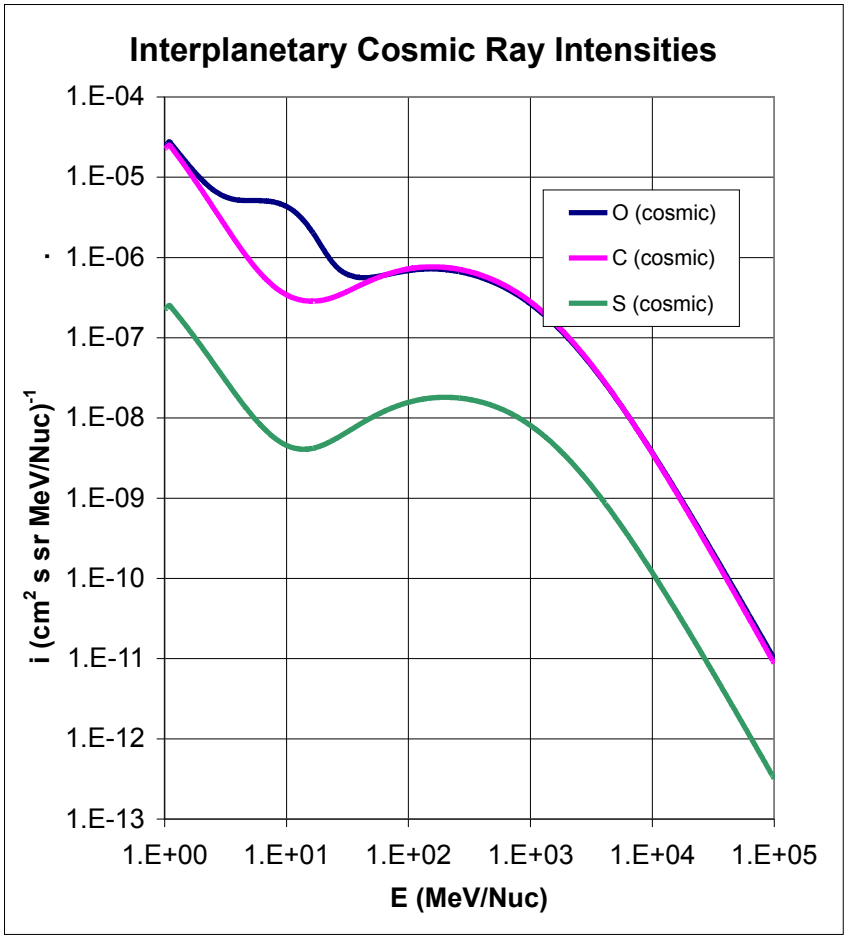

Fig. 7. Interplanetary galactic cosmic ray fluxes external to Jupiter at 5.9 AU.

DATA COMPARISONS

Mauk et al. (2004) have combined lower energy Galileo Energetic Particle Detector (EPD) data into estimates of the heavy ion fluxes over a wide range of energies (~50 KeV to ~50 MeV). Although their results are for a limited number of orbits and locations (the HIC values are averaged over many orbits and positions) and the EPD and HIC energy ranges do not quite overlap, they are amenable to comparison with the HIC oxygen and sulfur models. Three positions corresponding to the EPD orbit fits reported by Mauk et al. (2004) are plotted in Fig. 8. The agreement between the models appears to be consistent for oxygen if the EPD data were to be extrapolated to higher HIC energies. There may be differences, however, between the EPD and the HIC sulfur spectra as the HIC spectra are flattened at the lower end of their modeled energy range—the differences appear to increase as we move outward from 9.5 to 15 R_j. The reason for this discrepancy is not immediately clear. A detailed Geant4 Monte Carlo analysis of the geometric factors carried out by one of us (S. Kang) suggests that although the HIC LETB sulfur channel counted sulfur ions nearly uniformly over the expected energy range (see Appendix IV, Fig. A8), that range might be better estimated by assuming a low energy cut-off at ~7 MeV/nuc which would exclude the sulfur points below 9 MeV/nuc. The HIC sulfur model is, however, the least statistically certain (when compared to HIC carbon and oxygen) of our models. This suggests that the model may be incorrectly estimating the lower energy sulfur flux although lower statistical certainty generally leads to larger error estimates, not consistently lower average fluxes. It is also entirely plausible that the modeled sulfur inflections are real.

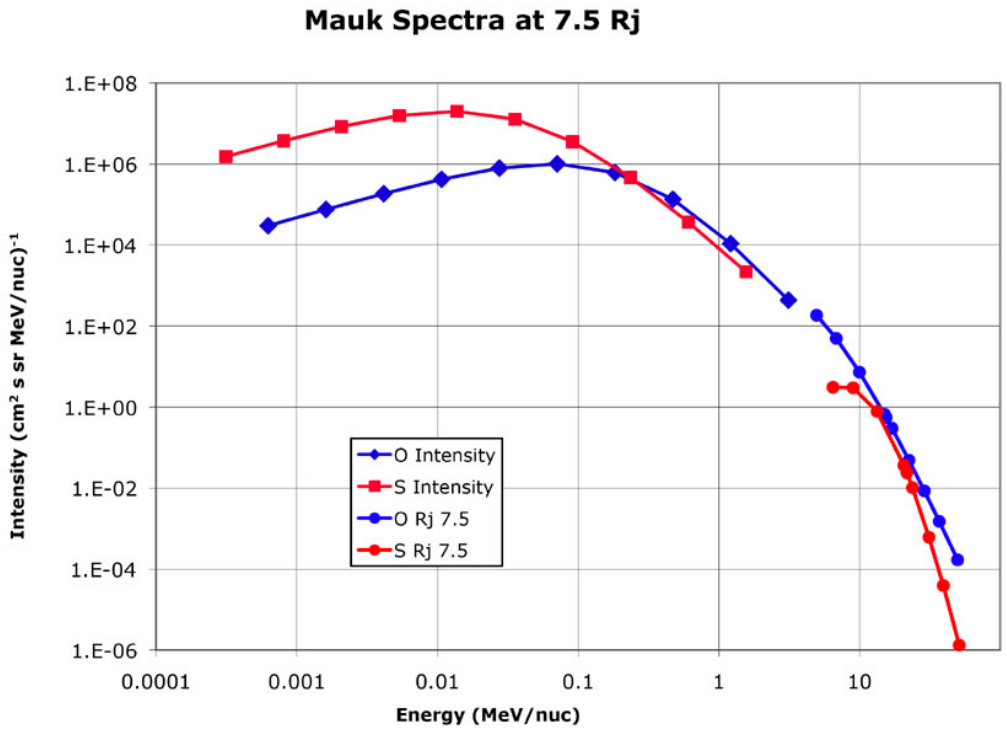

Fig. 8A. Comparisons between the modeled HIC data and Mauk et al. (2004) at 7.5 R_J (orbit JOI-1)

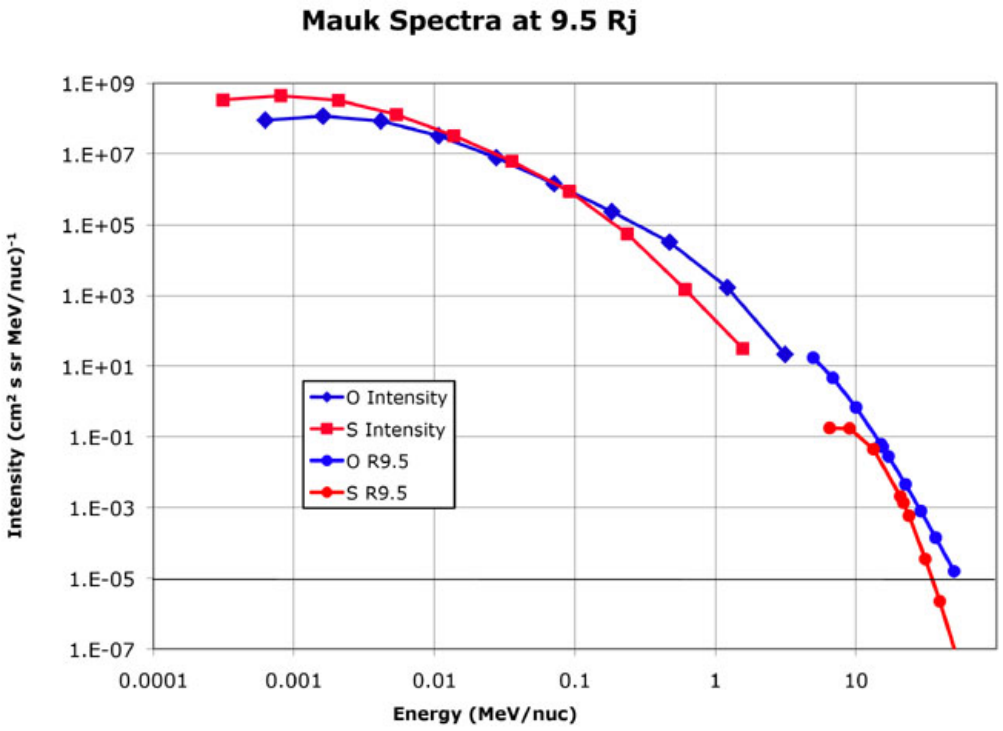

Fig. 8B. Comparisons between the modeled HIC data and Mauk et al. (2004) at 9.5 R_J (orbit E6_Enc).

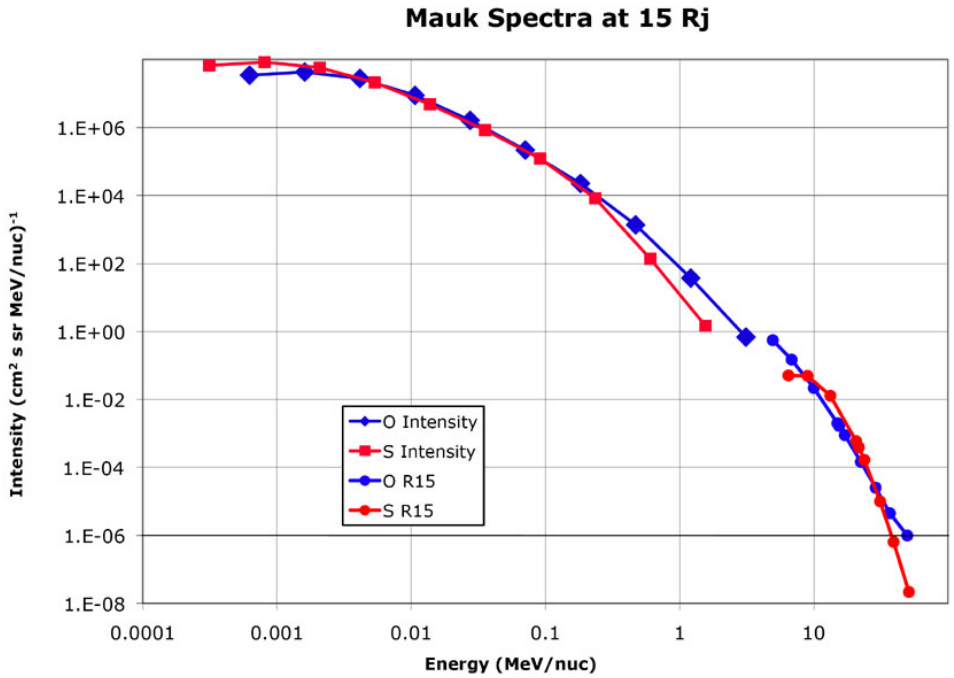

Fig. 8C. Comparisons between the modeled HIC data and Mauk et al. (2004) at 15 R_J (orbit G2_Enc).

INTEGRAL FLUENCES

Figure 9 illustrates the HIC integral fluence spectrum (particles/cm^2) for a Europa Orbiter-like mission profile (taken from a JPL Navigation Spice orbit scenario labeled "EO-9935_earth-to-EOI.bsp" that was a baseline example used in an earlier Europa orbit design study at JPL). As can be seen from Fig. 9, all these ion fluences and their totals are close to or equal to GCR values past ~30 MeV/nuc. The near-horizontal lines correspond to the external GCR environment. The bold lines are the combination of these two environments assuming that somewhere above 30 MeV/nuc the external GCR environment will penetrate the jovian magnetosphere. The cosmic ray spectra (Fig. 7) are so flat in energy in the range being modeled that the energy at which the GCR penetrate does not greatly affect the fluence (the integral from 100 MeV/nuc to infinity is approximately twice the integral from 1 GeV/nuc to infinity). The model assumes that the GCR above ~30 MeV/nuc penetrate the magnetosphere (i.e., the integral of the differential flux past 30 MeV/nuc is continued using the external GCR environment to estimate the integral fluxes and fluences).

Note that the external cosmic ray oxygen and carbon fluxes overlay each other. Also note that sulfur dominates carbon at intermediate energies. The oxygen from the GCR background is labeled "OXYGEN CR," and the total of HIC oxygen and GCR oxygen is labeled "OXYGEN HIC+CR". Carbon, sulfur, and total fluences are labeled similarly. The line labeled "TOTAL HIC+CR" is the combination of oxygen, carbon, and sulfur from the HIC model and the CRÈME 96 Cosmic Ray model.

Figure 10 is an estimate of the Galileo HIC model worst case Heinrich flux versus linear energy transfer (LET) for Europa Orbiter mission profile EO-9935. The LET flux is for 25 mils of aluminum shielding. The rapid fall-off in the carbon (~4), oxygen (~6), and sulfur (~20) LET spectra are typical for the Heinrich fluxes for these species and indicate that parts with an LET above ~30 MeV-cm^2/mg should be relatively immune to SEUs from these species (note: the background GCR are included in the Fig. 10 spectra).

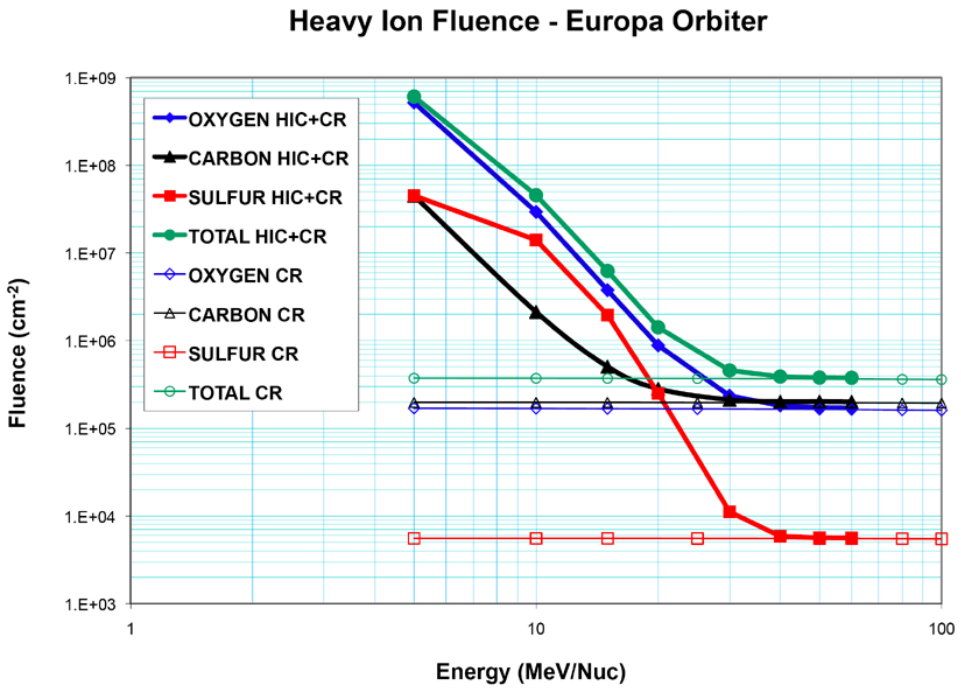

Fig. 9. Galileo HIC model and GCR heavy ion fluences for a mission to Europa. The mission is based on Europa Trajectory "EO9935." "CR" stands for the GCR component in the legend.

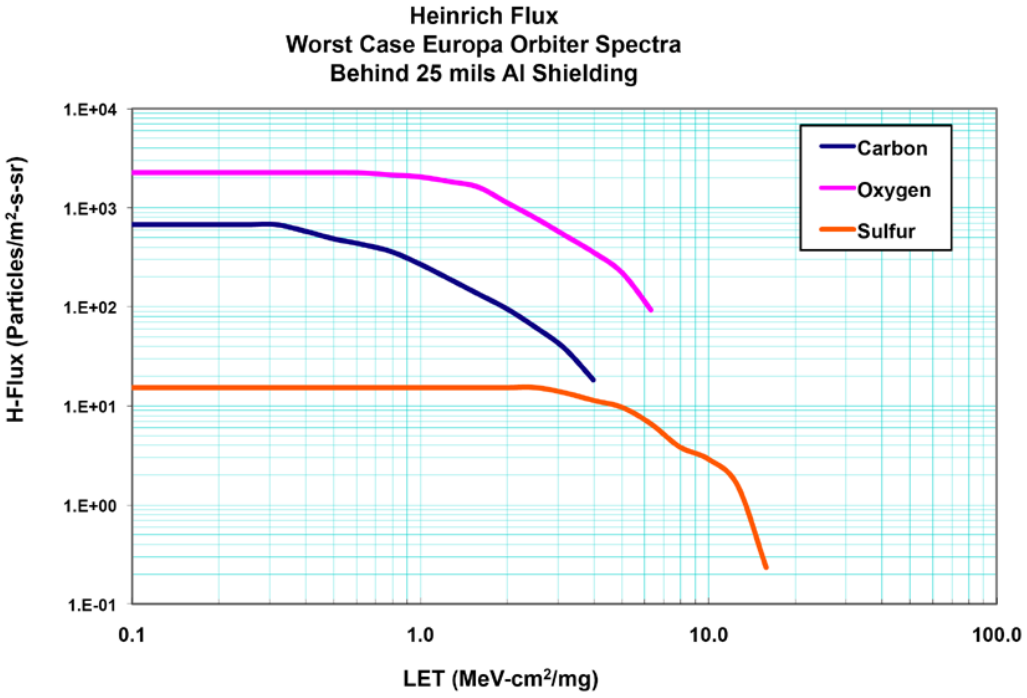

Fig. 10. Galileo HIC model worst case Europa Orbiter Heinrich flux versus LET. Flux is for 25 mils of aluminum shielding.

CONCLUSIONS

A quantitative model of the jovian equatorial heavy ion radiation environment has been developed based on data from the Galileo HIC experiment. The data covered the period 1995 to 2003 and included orbits C03 through J35 (excluding J5, J13, and A34) and the heavy ion range from $_{6}$C to $_{28}$Ni. The model defines the fluxes for oxygen (5–40 MeV/nuc), carbon (5-40 MeV/nuc), and sulfur (6.3–40 MeV/nuc) between ~5–25 R_J. Average differential flux spectra for these three components are presented in terms of energy for selected radial bins. A simple fit has been developed in terms of energy and radial distance that allows interpolation of the fluxes at intermediate values of the two variables. As the model is based on averages over pitch angle from Galileo, which primarily orbits in the jovian equatorial plane, the model is considered valid for approximately 2–3 R_J above or below that plane between 5–25 R_J. The model defaults to the ambient GCR levels for carbon, oxygen, and sulfur values for fluxes below 10^{-6} $(cm^2\ s\ sr\ MeV/nuc)^{-1}$ for carbon and oxygen and 10^{-8} $(cm^2\ s\ sr\ MeV/nuc)^{-1}$ for sulfur.

REFERENCES

Cohen, C. M. S., T. L. Garrard, E. C. Stone, J. F. Cooper, N. Murphy, and N. Gehrels, "Io encounters past and present: A heavy ion comparison", *J. Geophys. Res.,* vol. 105, no. A4, pp. 7775-7782, 2000.

Cohen, C. M. S., E. C. Stone, and R. S. Selesnick, "Energetic ion observations in the middle Jovian magnetosphere", *J. Geophys. Res.*, vol. 1066, no A12, pp. 29,871–29,881, 2001.

Connerney, J. E. P., M. H. Acuna, N. F. Ness, T. Satoh, "New models of Jupiter's magnetic field constrained by the Io flux tube footprint", *J. Geophys. Res.,* Vol. 103, A6, 11929-11940, 1998.

Divine, N., "Jupiter oxygen Ion Spectra," JPL IOM-5137-83-279, Jet Propulsion Laboratory, Pasadena, CA, Nov. 11, 1983.

Divine, N., "Energetic Heavy Ion Fluxes for Jupiter Flybys," JPL IOM-5215-92-024, Jet Propulsion Laboratory, Pasadena, CA, June 10, 1992.

Evans, R. W., H. B. Garrett, C. M. S. Cohen, and E. C. Stone, "Galileo Heavy Ion Radiation Model" (Abstract), *American Geophysical Union Fall Meeting*, San Francisco, CA, December 6, 2006.

Evans, R. W., H. B. Garrett, I. Jun, C. M. S. Cohen, E. C. Stone, and S. J. Drouilhet, "The Galileo Heavy Ion Environment—Update to the HIC Model" (Abstract), *American Geophysical Union Fall Meeting*, San Francisco, CA, December 2007.

Garrard, T. L., N. Gehrels, and E. C. Stone, "The Galileo Heavy Element Monitor", *Space Sci. Rev.,* vol. 60, pp. 305–315, 1992. (Also available as SRL publication 91-08.)

Garrett, H. B., I. Jun, J. M. Ratliff, R. W. Evans, G. A. Clough, and R.W. McEntire, *Galileo Interim Radiation Electron Model*, JPL Publication 03-006, 72 pages, The Jet Propulsion Laboratory, California Institute of Technology, Pasadena, CA, 2003. http://www.openchannelfoundation.org/projects/GIRE/.

Gehrels, N., E. C. Stone, and J. H. Trainor, "Energetic oxygen and sulfur in the Jovian Magnetosphere", *J. Geophys. Res.*, vol. 86, no. A11, pp. 8906–8918, 1981.

Gehrels, N., and E. C. Stone, "Energetic oxygen and sulfur in the Jovian Magnetosphere and Their Contribution to the Auroral Excitation", *J. Geophys. Res.*, vol. 88, no. A7, pp. 5537–5550, 1983.

Mauk, B. H., D. G. Mitchell, R. W. McEntire, C. P. Paranicas, E. C. Roelof, D. J. Williams, and S. M. Krimigis, "Energetic ion characteristics and neutral gas interactions in Jupiter's magnetosphere", *J. Geophys. Res.*, vol. 109, A09S12, doi:10.1029/2003JA010270, 2004.

Paranicas, C., B. H. Mauk, J. M. Ratliff, C. Cohen, R. E. Johnson, "The ion environment near Europa and its role in surface energetics", *Geophys. Res. Lttrs.*, vol. 29, no. 5, p. 1074, 10.1029/2001GL014127, 2002.

Roederer, J. G., "Dynamics of Geomagnetically Trapped Radiation," *Physics and Chemistry in Space*, Vol. 2, Springer-Verlag, New York, New York, 166 pages, 1970.

APPENDICES

APPENDIX I. Estimated Errors and Number of Points for Carbon

The following tables include the number of estimated errors, the number of non-zero points, and the total number of data points for the carbon data.

Table IA. Carbon Estimated Errors

Energy (MeV/nuc)	R5.5-6.5	R6.5-7.5	R7.5-8.5	R8.5-11.	R11.-13.	R13.-17.	R17.-25.
4.359	2.98E+00	8.03E+00	3.29E+00	2.08E-01	1.12E-01	1.21E-02	1.51E-03
5.916	1.41E+00	5.81E+00	2.27E+00	1.92E-01	9.54E-02	1.26E-02	1.26E-03
8.532				3.45E-02	1.29E-02	1.54E-03	1.85E-04
14.239	1.71E-02	6.27E-02	1.36E-02	3.30E-04	2.91E-04	9.34E-05	3.10E-06
15.955		1.29E-02	4.79E-03	8.91E-05	7.30E-05	1.06E-05	
26.397	9.02E-04	1.17E-03	1.74E-04	6.21E-06	7.62E-06	2.79E-06	1.32E-06
33.071			7.03E-05	3.12E-06	4.33E-06	4.35E-06	

Table IB. Carbon Number of Non-Zero Values

Energy (MeV/nuc)	R5.5-6.5	R6.5-7.5	R7.5-8.5	R8.5-11.	R11.-13.	R13.-17.	R17.-25.
4.359	9	29	13	96	115	301	348
5.916	9	24	24	177	177	533	403
8.532	2	0	2	11	7	111	142
14.239	20	33	48	318	159	60	6
15.955	3	14	14	117	50	16	4
26.397	8	6	22	101	39	15	11
33.071	1	4	15	34	11	6	2

Table IC. Carbon Number of Values

Energy (MeV/nuc)	R5.5-6.5	R6.5-7.5	R7.5-8.5	R8.5-11.	R11.-13.	R13.-17.	R17.-25.
4.359	67	106	117	917	557	973	1036
5.916	67	106	117	917	557	973	1036
8.532	67	106	117	917	557	973	1036
14.239	67	106	117	815	463	838	1013
15.955	67	106	117	815	463	838	1013
26.397	54	53	112	553	242	497	929
33.071	54	53	112	553	242	497	929

APPENDIX II. Estimated Errors and Number of Points for Oxygen

The following tables include the number of estimated errors, the number of non-zero points, and the total number of data points for the oxygen data.

Table IIA. Oxygen Estimated Errors

Oxygen Estimated Errors

Energy (MeV/nuc)	R5.5-6.5	R6.5-7.5	R7.5-8.5	R8.5-11.	R11.-13.	R13.-15.	R15.-17.	R17.-25.
4.951	1.24E+01	1.36E+01	7.11E+00	4.59E-01	2.32E-01	7.55E-02	1.08E-02	1.57E-03
6.837	3.73E+00	7.06E+00	4.46E+00	2.53E-01	1.22E-01	2.44E-02	7.59E-03	1.12E-03
10.002	1.38E+00	2.49E+00	1.11E+00	6.88E-02	3.13E-02	5.91E-03	1.72E-03	2.72E-04
17.051	3.49E-02	9.00E-02	2.74E-02	5.50E-04	2.80E-04	2.26E-04	2.68E-05	3.32E-06
22.454	7.54E-03	1.62E-02	4.67E-03	1.10E-04	5.39E-05	3.62E-05	6.45E-06	3.71E-07
28.912	6.45E-04	1.64E-03	3.56E-04	1.42E-05	1.08E-05	7.94E-06	1.08E-06	3.72E-07
36.889	7.36E-05	6.10E-04	1.10E-04	2.67E-05	7.92E-06	6.17E-06	3.43E-06	1.20E-06

Table IIB. Oxygen Number of Non-Zero Values

Energy (MeV/nuc)	R5.5-6.5	R6.5-7.5	R7.5-8.5	R8.5-11.	R11.-13.	R13.-15.	R15.-17.	R17.-25.
4.951	63	61	73	483	314	307	315	514
6.837	42	45	71	417	313	359	349	468
10.002	23	26	28	103	83	150	163	189
17.051	67	106	117	596	269	81	19	11
22.454	65	97	114	495	189	57	11	5
28.912	49	37	107	270	77	30	6	32
36.889	27	19	50	122	24	11	6	26

Table IIC. Oxygen Number of Values

Energy (MeV/nuc)	R5.5-6.5	R6.5-7.5	R7.5-8.5	R8.5-11.	R11.-13.	R13.-15.	R15.-17.	R17.-25.
4.951	67	106	117	917	557	510	463	1036
6.837	67	106	117	917	557	510	463	1036
10.002	67	106	117	917	557	510	463	1036
17.051	67	106	117	815	463	415	423	1013
22.454	67	106	117	815	463	415	423	1013
28.912	54	53	112	553	242	210	287	929
36.889	54	53	112	553	242	210	287	929

APPENDIX III. Estimated Errors and Number of Points for Sulfur

The following tables include the number of estimated errors, the number of non-zero points, and the total number of data points for the sulfur data.

Table IIIA. Sulfur Estimated Errors

Energy (MeV/nuc)	R5.5-6.5	R6.5-7.5	R7.5-8.5	R8.5-9.5	R9.5-13.	R13.-17.	R17.-25.
6.481		2.80E+00	1.33E+00	2.24E-01	4.03E-02	4.18E-03	2.62E-05
9	1.07E+00	1.66E+00	8.14E-01	6.99E-02	2.37E-02	1.84E-03	2.34E-05
13.309	3.94E-01		2.10E-01	3.08E-02	5.02E-03	1.11E-04	
23.824	2.71E-03	6.54E-03	1.19E-03	1.38E-04	9.84E-06		
31.146	6.19E-04	1.91E-03	4.38E-04	7.13E-06			
39.444			9.23E-06				

Table IIIB. Sulfur Number of Non-Zero Values

Energy (MeV/nuc)	R5.5-6.5	R6.5-7.5	R7.5-8.5	R8.5-9.5	R9.5-13.	R13.-17.	R17.-25.
6.481	0	10	8	18	47	45	33
9	17	9	10	12	40	63	30
13.309	11	1	4	5	9	6	3
23.824	19	20	18	23	12	1	0
31.146	13	25	11	11	2	2	1
39.444	3	3	5	2	2	1	1

Table IIIC. Sulfur Number of Values

Energy (MeV/nuc)	R5.5-6.5	R6.5-7.5	R7.5-8.5	R8.5-9.5	R9.5-13.	R13.-17.	R17.-25.
6.481	67	106	117	917	557	973	1036
9	67	106	117	917	557	973	1036
13.309	67	106	117	917	557	973	1036
23.824	67	106	117	815	463	838	1013
31.146	67	106	117	815	463	838	1013
39.444	54	53	112	553	242	497	929

APPENDIX IV. Monte Carlo Simulations of the Galileo Heavy Ion Counter

S. Kang

INTRODUCTION

Monte Carlo radiation transport studies were performed using the Geant4 radiation transport code (Version 9.1.p02 [Agostinelli et al., 2003]) for the Galileo spacecraft heavy ion counter (HIC) to evaluate its response to energetic carbon, oxygen, and sulfur ions. The HIC consists of two solid-state detector telescopes named Low Energy Telescopes (LET B and LET E; see [Garrard et al., 1992]). These two telescopes were optimized for the detection of nuclei with different energy levels. LET B was designed to detect lower energy nuclei down to about 6 MeV/nuc and LET E to detect energies as high as 200 MeV/nuc. LET B measured heavy ion fluxes with energy thresholds of 0.3, 0.4, 3.7, and 2.0 MeV using its four detectors. LET E measured heavy ion fluxes with energy thresholds of 9.3, 2.0, 25, and 117 MeV (detector 4 and detector 5 have the same energy threshold) using its five detectors. The calculation results are presented in the form of "geometric factors" for the heavy ions energy thresholds for each telescope. The geometric factor is the energy-dependent detector response function that relates the incident particle fluxes to instrument count rates. The Geant4 simulation results generally show good agreement with the original predictions made by using a standard "telescope equation" [Garrard et al., 1992] and range tables, plus they provide additional refinements in the energy ranges that help in interpreting the data collected by the HIC particle telescopes.

GEANT4 MASS MODEL

Detailed mass models of the LET B and LET E have been developed for Geant4 [Agostinelli et al., 2003]. The referenced mass models on which the LET B and LET E Geant4 models were constructed for the transport analyses were derived from detailed drawings provided by the NASA Goddard Space Flight Center [Anon., 1991a,b]. The descriptions of each model are presented below.

LET B

The LET B was designed to detect lower energy nuclei down to about 6 MeV/nuc and contains four solid state silicon detectors. The silicon detector names, their physical size in terms of thickness and radius, and their threshold energy levels (defined as the minimum energy required for the silicon detector to measure ions) are shown in Table IVA. The LET B has only one channel logic requirement and it is expressed as LB1.LB2.LB3!LB4. It means that, to be recorded by the LET B telescope, the ion has to deposit energy greater than the threshold energy in the detectors LB1, LB2, and LB3 but not in LB4. Figure A1 presents a Geant4 mass model of the LET B telescope. The figure shows the same mass model depicted in different formats to reveal the locations of the four silicon detectors (left) and the outer surface (right).

Table IVA. LET B Telescope Detector Description.

Detector Name	Detector Radius (cm)	Detector Thickness (micron)	Energy Threshold (MeV)
LB1	0.95	32.1	0.3
LB2	0.95	29.6	0.4
LB3	1.13	421	3.7
LB4	1.13	440	2

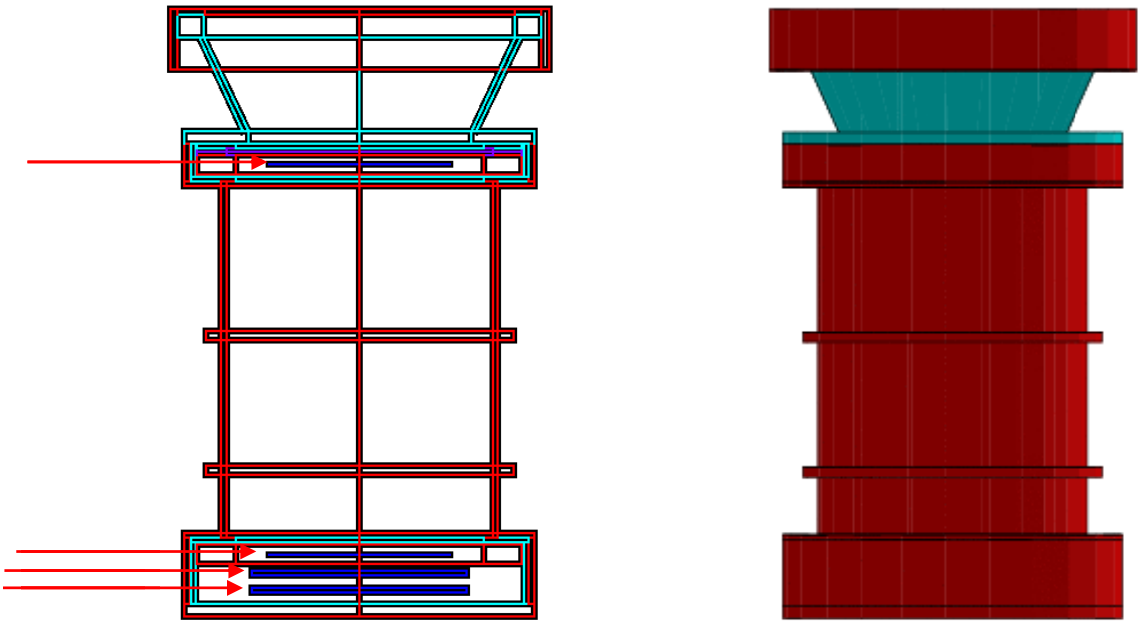

Fig. A1. Geant4 model of the LET B Telescope.

LET E

The LET E was designed to measure heavy ion fluxes with energy thresholds of 9.3, 2.0, 25, and 117 MeV (detector 4 and detector 5 have the same energy threshold) using its five detectors. The silicon detector names, their physical size in terms of thickness and radius, and their threshold energy levels (defined as the minimum energy required for the silicon detector to measure ions) are shown in Table IVB. The LET E has four logic channel requirements named DUBL, TRPL, WDSTP, and WDPEN. The DUBL means that ions are detected at LE1 and LE2 but not at LE3 with the energy deposition in each detector higher than the threshold level specified in Table IVB. The TRPL means that ions are detected at LE1, LE2, and LE3 but not in LE4 with the energy deposition in each detector higher than the threshold level specified in Table IVB. The WDSTP and WDPEN channels follow the same concepts as DUBL and TRPL except that LE4 also has to be detected for WDSTP and LE5 for WDPEN. Table IVC summarizes the logic.

Table IVB. LET E Telescope Detector Description.

Detector Name	Detector Radius (cm)	Detector Thickness (micron)	Energy Threshold (MeV)
LE1	0.95	30.4	9.3
LE2	0.95	33.4	2
LE3	1.13	463	25
LE4	1.66	2000	117
LE5	1.66	2000	117

Table IVC. LET E Telescope Detector Channel Logic.

Logic Name	Chanel Logic Requirement
DUBL	LE1.LE2.!LE3
TRPL	LE1.LE2.LE3.!LE4
WDSTP	LE2.LE3.LE4.!LE5
WDPEN	LE2.LE3.LE4.LE5

Figs. A2a and A2b are the Geant4 mass model for the LET E telescope. These are the same mass model depicted in different formats to reveal the locations of the five silicon detectors (A2a) and to show the outer surface (A2b).

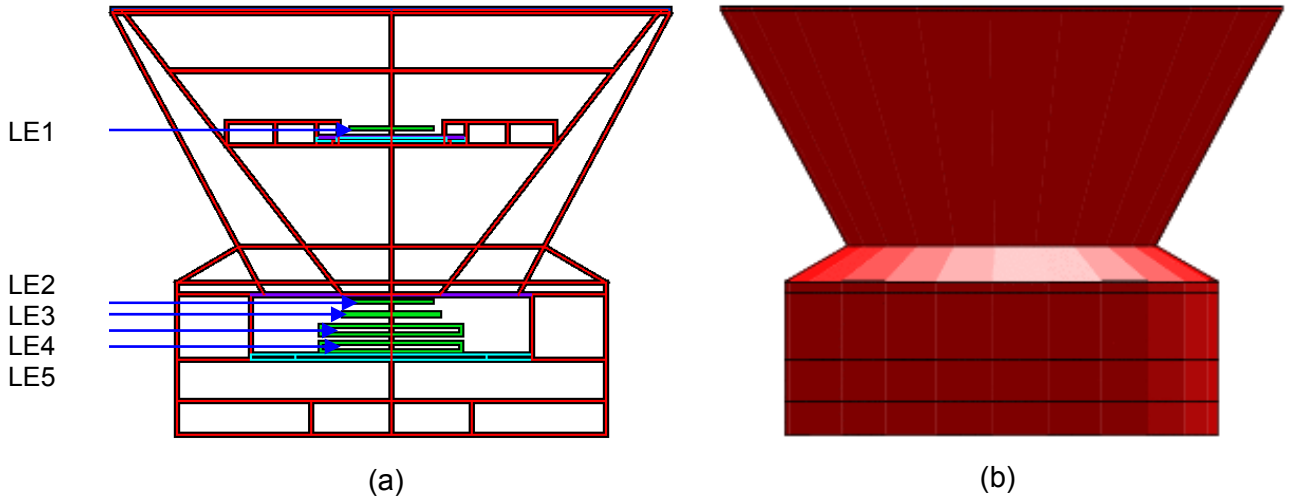

Fig. A2. Geant 4 model of the LET E Telescope

GEOMETRIC FACTOR

The goal of the Geant4 simulation is to calculate "geometric factors" for the carbon, oxygen, and sulfur ions for each telescope (LET B and LET E). The geometric factor is a combination of detector efficiency and solid angle subtended by the detector. In essence, it is the detector's response function. It can be computed, for a specific channel, as the ratio of the number of particles satisfying the channel logic to the number of source particles simulated per unit area, and multiplied by 4π. This multiplication is necessary to account for the source particles from the full 4π space. Then, the geometric factor can be expressed as shown below.

$$\text{Geometric Factor} = \frac{\text{\# of Particles detected by real detector}}{\text{\# of Particles generated per unit area}} * 4\ \text{Pi}$$

GEANT4 SIMULATION PROCESS AND RESULTS

The Geant4 simulation of ions that satisfies the conditions as described above required setting up several source codes. Table IVD provides descriptions of the some of the key source codes and their applications.

Table IVD. Geant4 Physics and Model setup.

Source Code Name	Application
DetectorConstruction.cc	The physical model was built using this source code including the dimensions and material.
PrimaryGeneratorAction.cc	G4GeneralParticleSource(GPS) functions were used. The GPS allows the specification of incident sources. For example, a 120-MeV carbon ion from a spherical source with a cosine distribution can be specified.
PhysicsList.cc	G4ionIonisation and G4hMultipleScattering were specified in the standard EM physics to correctly transport heavy ions.
SteppingVerbose.cc	The code was modified to generate the output for the particles only when they traverse the telescopes' detectors to avoid generating output files that were too large to control.

GEANT4 TRANSPORT ANALYSIS RESULT

To validate the model's integrity and check the applicability and capability of the incorporated physics routines, namely G4ionIonisation and G4hMultipleScattering, prior to the full analysis, several simple beam analyses were performed first. These beam analyses were performed on the same mass model and for the same physics except for the source particle generation. The beam analysis results were then compared with the ion range tables generated using the Transport of Ions in Matter (TRIM) code (version 2008), which is a collection of software packages that calculate the transport of ions in matter [Ziegler, 2011].

ION BEAM CASE STUDY USING LET E

The LET E was chosen for the beam analysis because it has more physical components and detectors compared to LET B. The first case of the beam studies was performed with the carbon ions having 11 MeV/nuc (132 MeV) incident energy. The beam comes down from the top of the telescope (as shown in Fig. A3) and transverses through the outer foil window (3 mils of Kapton) but is completely stopped by the inner foil window (10 mils aluminum). The TRIM calculation also shows that carbon ion energies between 10.8 MeV/nuc and 11.7 MeV/nuc are stopped by 11 mils of silicon. The next case analysis is performed with a 45-MeV/nuc (540 MeV) incident energy. In this case, the beam ion will traverse 10 mils of aluminum, 3 mils of kapton, and about 100 mils of the silicon detectors (1.2 mils of LE1, 1.3 mils of LE2, 18. 2 mils of LE3, and 78.7 mils of LE4). The TRIM cacluation shows that a carbon ion with 45 MeV/nuc will penetrate about 120 mils of silicon, and this matches well with the thickness that Geant4 computed. Figure A4 presents the Geant4 analysis using TRIM, a subset of the Stopping and Range of Ions in Matter (SRIM) calculation tables, for 45 MeV/nuc.

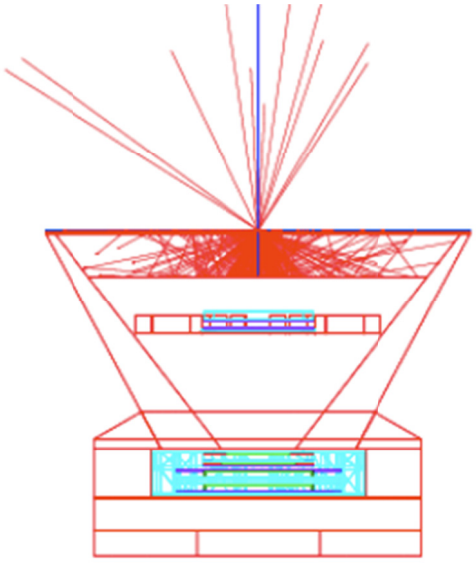

Energy (MeV/nuc)	Range (cm)	Range (mil)
10.8	0.0247	10
11.7	0.0280	11
12.5	0.0315	12
13.3	0.0352	14

Fig. A3. Visualization of Geant4 simulation for a carbon ion beam with incident energy of 11 MeV (table shows the TRIM Calculation Result).

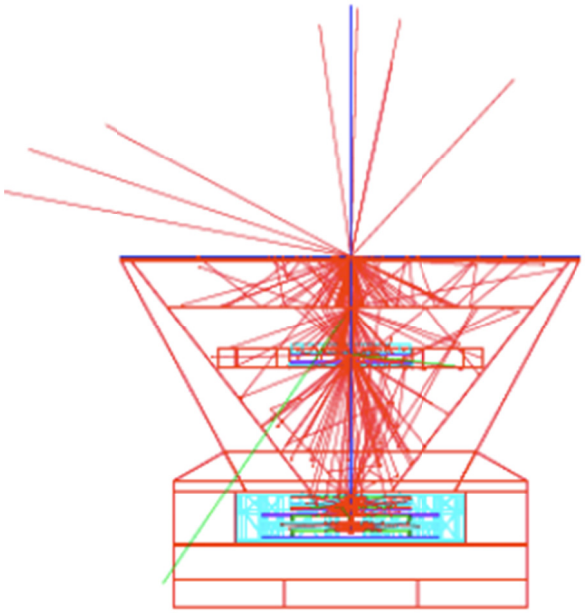

Energy (MeV/nuc)	Range (cm)	Range (mil)
37.5	0.2190	86
41.7	0.2640	104
45.8	0.3130	123
50.0	0.3650	144

Fig. A4. Visualization of Geant4 simulation for a carbon ion beam with incident energy of 45 MeV (table shows the TRIM Calculation Result).

GEANT4 SIMULATION OF SPACE ENVIRONMENT

The analysis then simulated the space environment conditions based on the confidence demonstrated by the simple beam cases. A series of detailed Monte Carlo calculations were performed to obtain the responses of the detectors as functions of incident particle energy. The energy ranges covered in the simulations are 24 MeV to 900 MeV for the LET B telescope and

96 MeV to 9.6 GeV for the LET E. The number of source particles simulated for each energy input is 1 million for both telescopes. Each ion was tracked from the point of the problem geometry until it completely lost energy. Fig, A5 provides a pictorial representation of the Geant4 simulation.

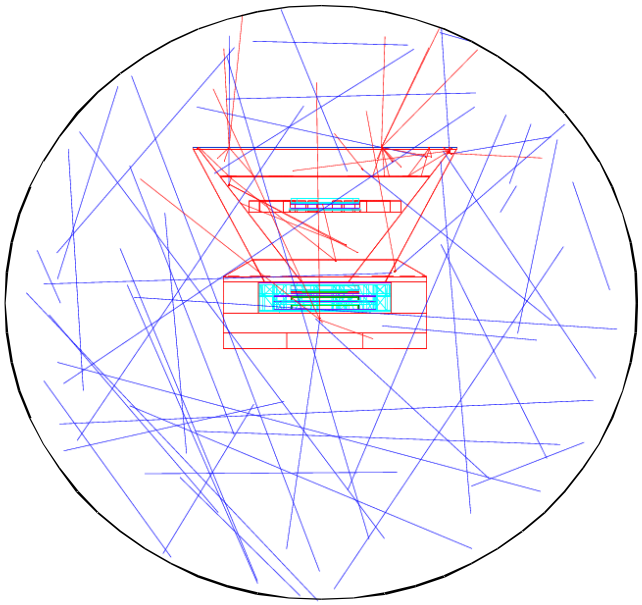

Fig. A5. Geant4 simulation. 50 carbon ions, shown as the blue lines, were injected. The red lines represent secondary particles that were also followed.

Geant4 Monte Carlo simulations such as this require intense computing power in terms of CPU and hard disk storage. The analyses were performed by utilizing a cluster system, named "ying." The ying cluster has 20 nodes and each node has two Intel(R) Xeon(R) CPU E5462 at 2.80 GHz. This CPU has quad cores such that all together 80 simulations were running independently at high speeds. Due to the size of output that each simulation generates by tracking primary ions and their secondary particles, sufficient hard disk space is crucial. The ying was equipped with 1 Tb of storage, which was extended even further by having teak (another Linux-based server) mounted.

Figures A6 through A26 present the Geant4 simulation results of the geometric factor analyses as functions of carbon, oxygen, and sulfur incident ion energies are presented. Also shown in each plot in addition to the Geant4 simulated values are the incident energy ranges provided by C. M. S. Cohen [private communications] and the geometric factors given by Garrard et al. [1992]. The data for the WDPEN cases were not provided by Cohen so these results were only compared with the Garrard et al. [1992] results. However, for the carbon WDPEN case, neither provided data (Figs. A13 and A14). As shown, the Geant4 simulation results show good agreement with the predictions by Cohen and Garrard et al. and also provide additional refinements for the energy ranges being studied which might help in better interpreting the data.

LET B TELESCOPE RESULTS

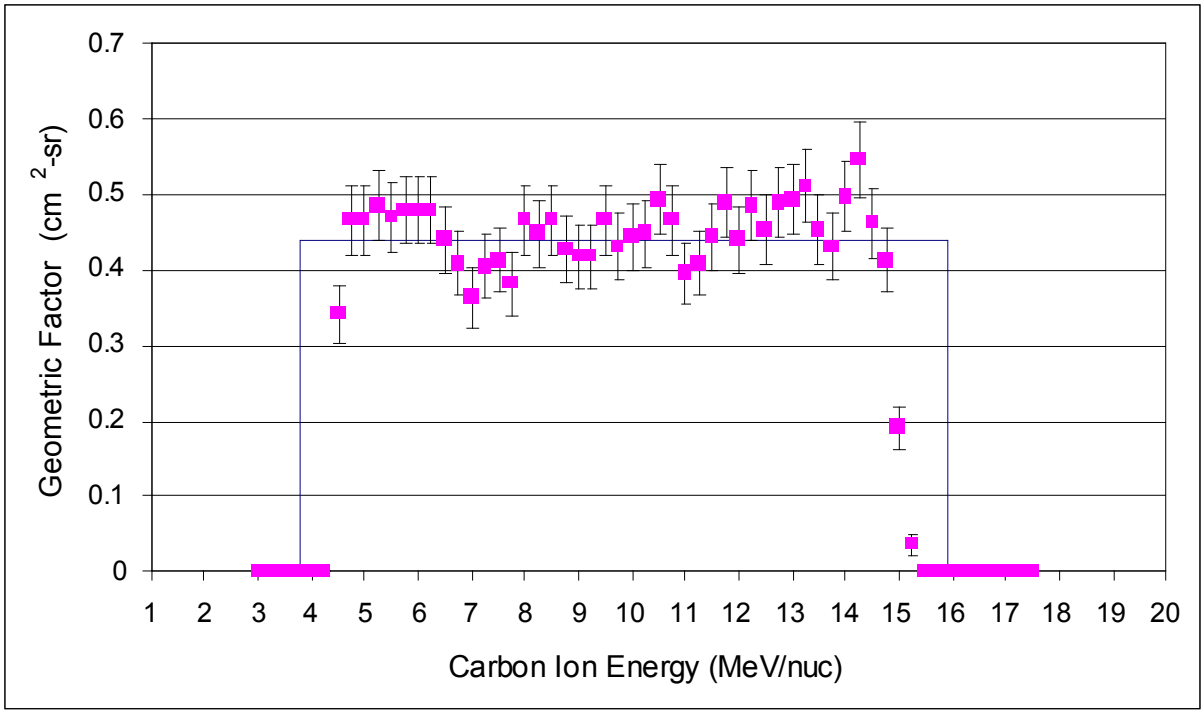

Fig. A6. LET B: Geant4 Simulation of Geometric Factor for the Carbon Ion

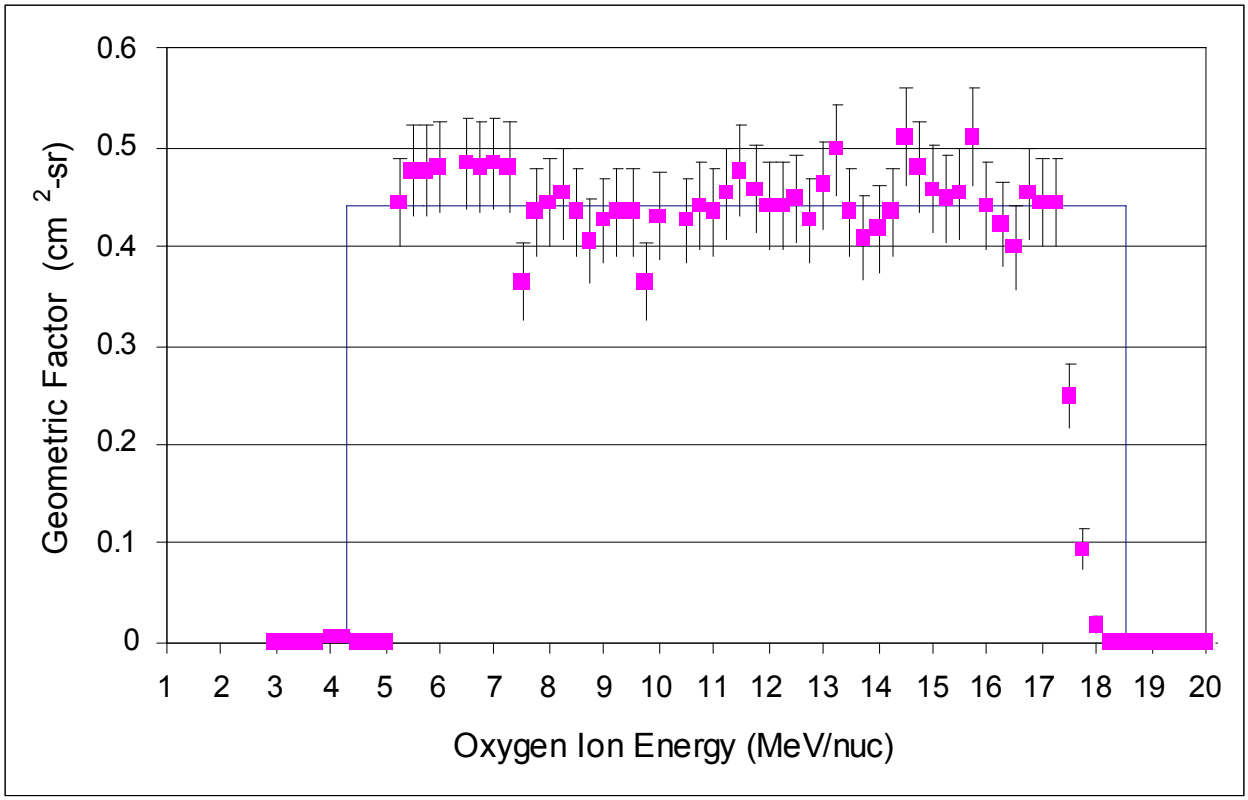

Fig. A7. LET B: Geant4 Simulation of Geometric Factor for the Oxygen Ion

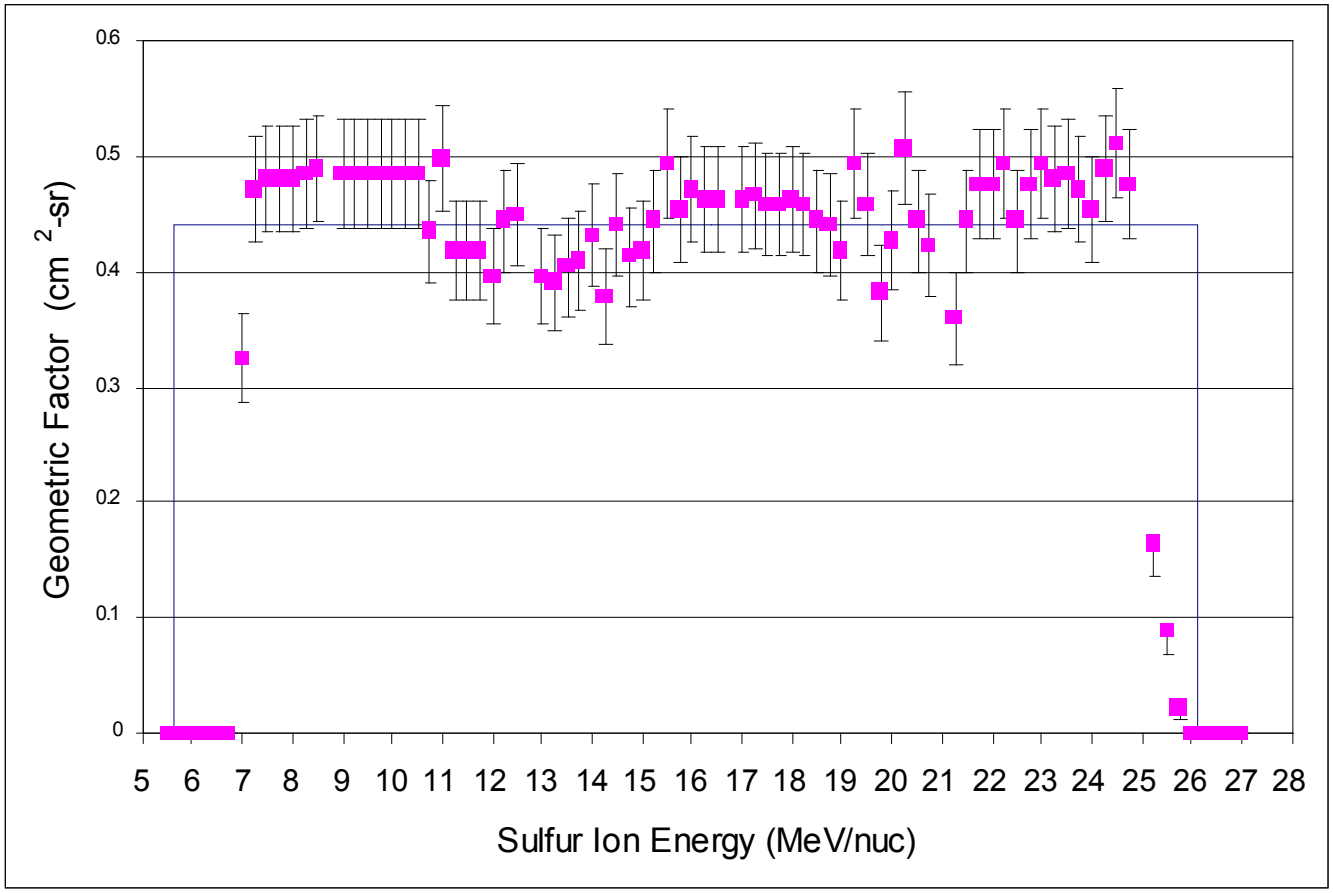

Fig. A8. LET B: Geant4 Simulation of Geometric Factor for the Sulfur Ion

LET E TELESCOPE RESULTS

CARBON ION

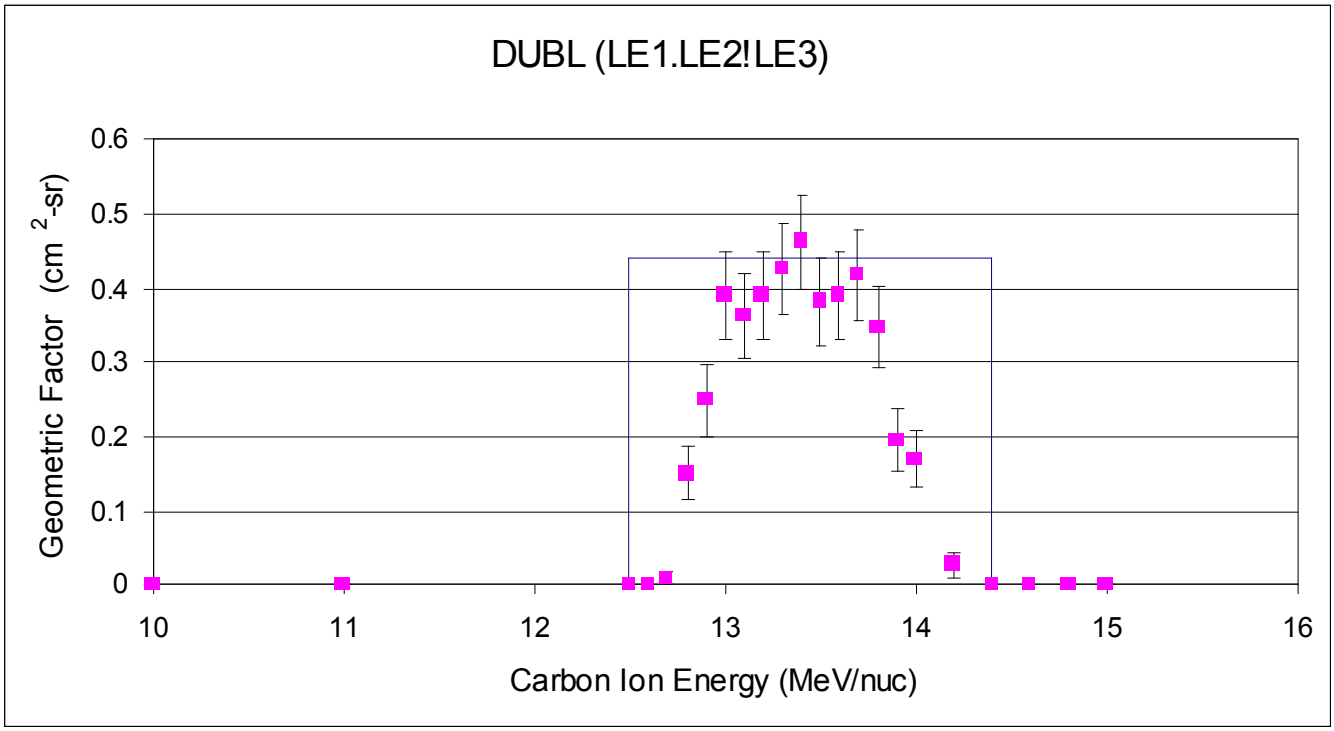

Fig. A9. LET E: Geant4 Simulation of Geometric Factor for the Carbon Ion for the DUBL logic.

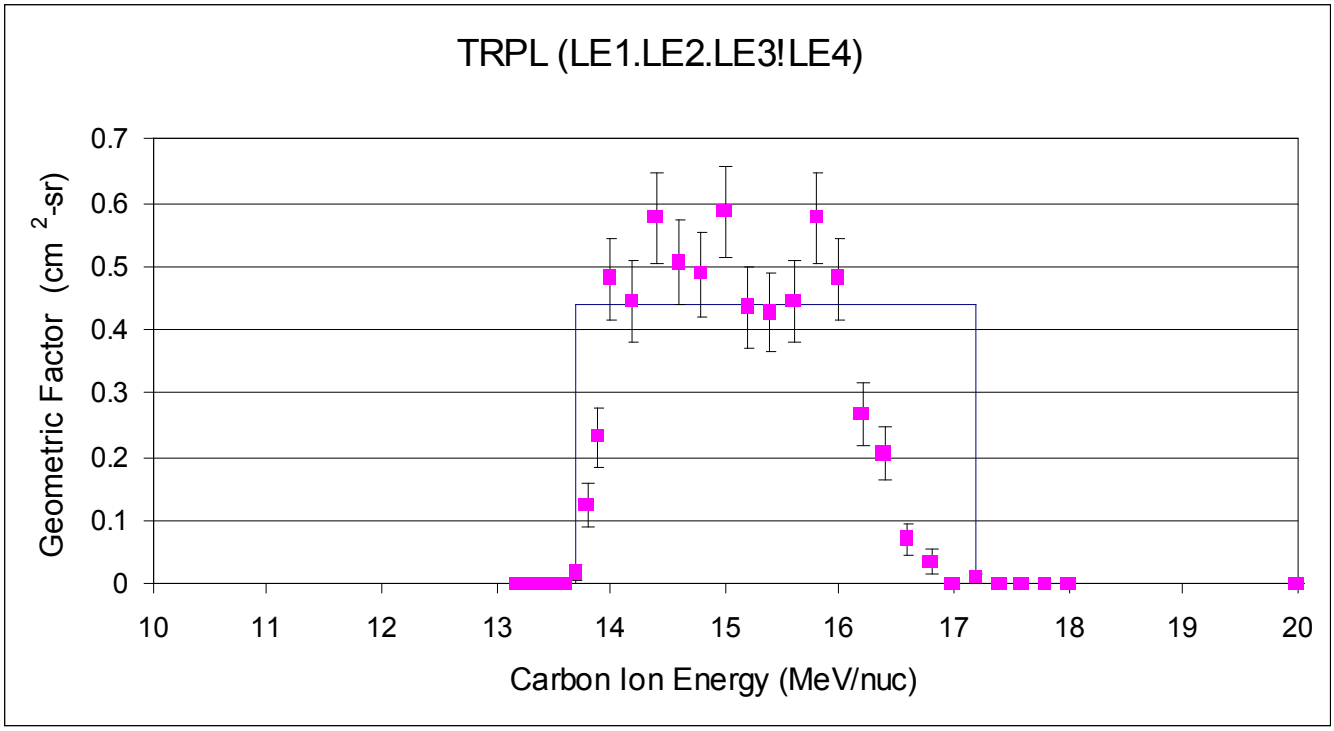

Fig. A10. LET E: Geant4 Simulation of Geometric Factor for the Carbon Ion for the TRPL logic.

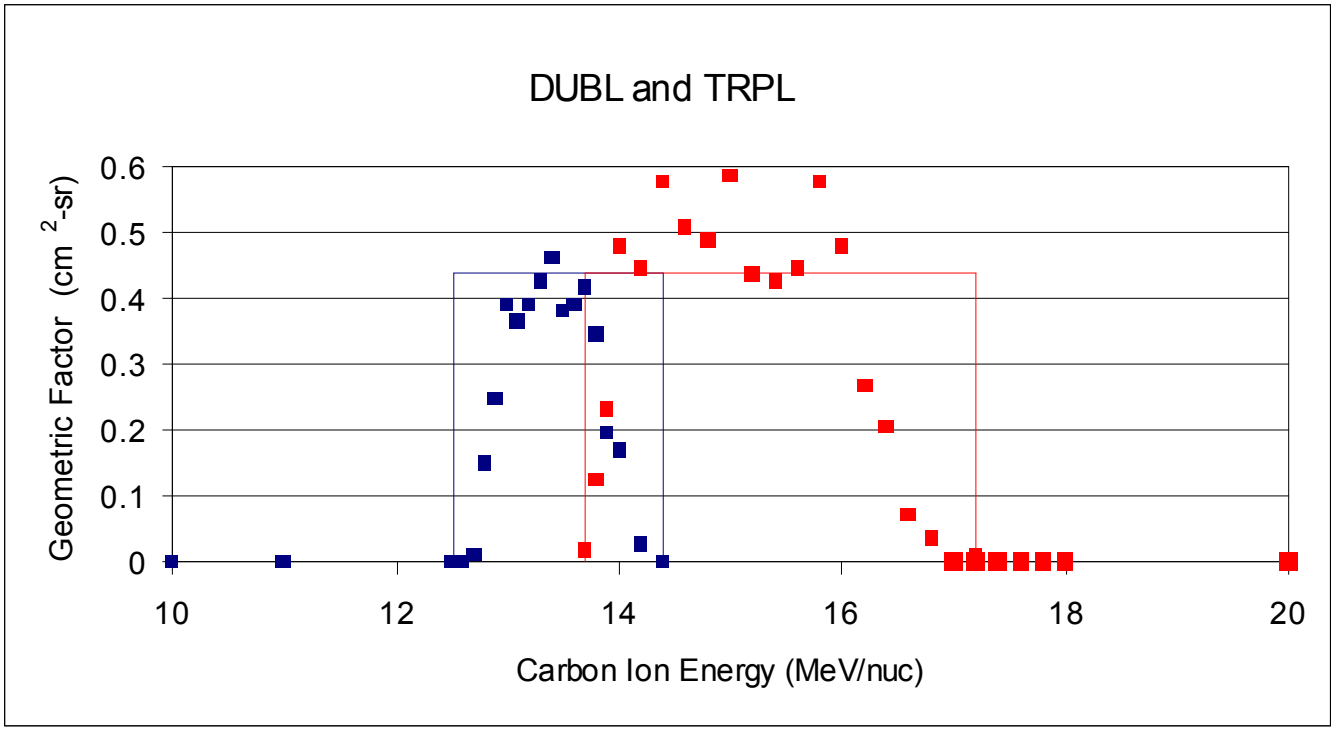

Fig. A11. LET E: Geant4 Simulation Result for DUBL (Fig. A9) and TRPL (Fig. A10) cases for the Carbon Ion (low energy cases). (blue squares = DUBL and red squares = TRPL)

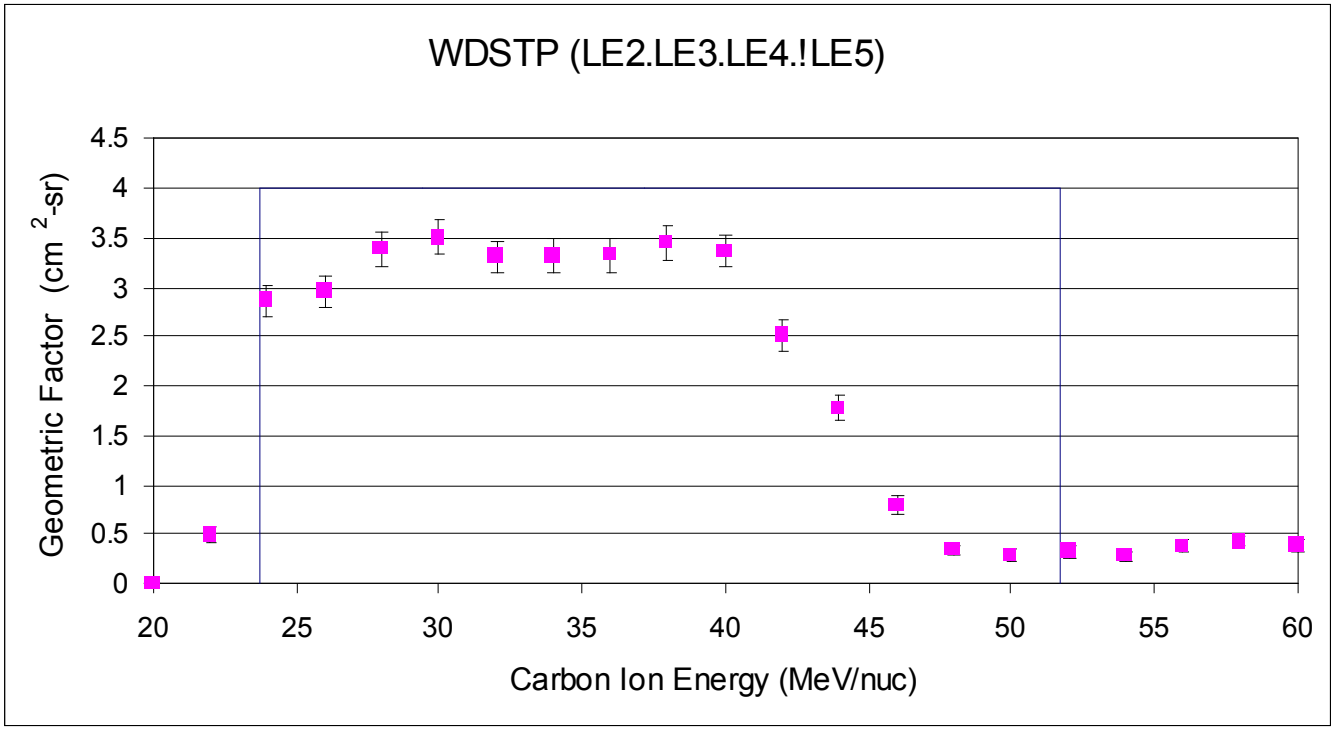

Fig. A12. LET E: Geant4 Simulation of Geometric Factor for the Carbon Ion for the WDSTP logic.

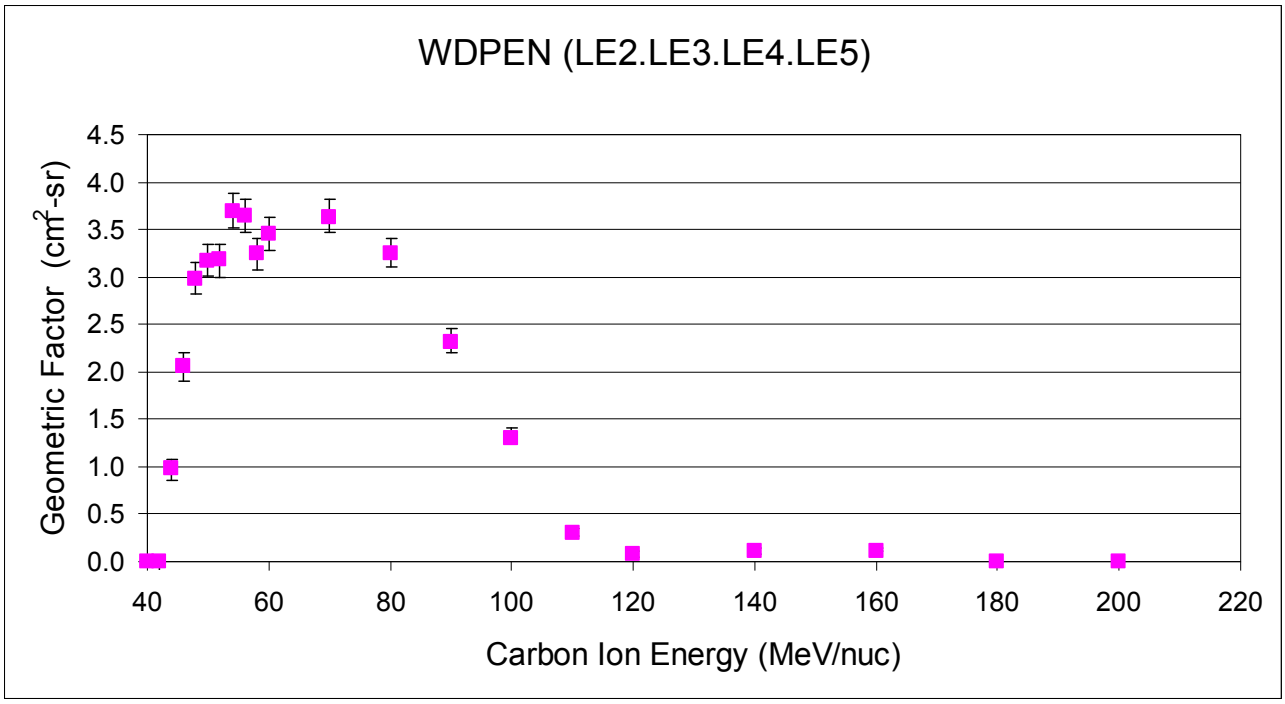

Fig. A13. LET E: Geant4 Simulation of Geometric Factor for the Carbon Ion for the WDPEN logic.

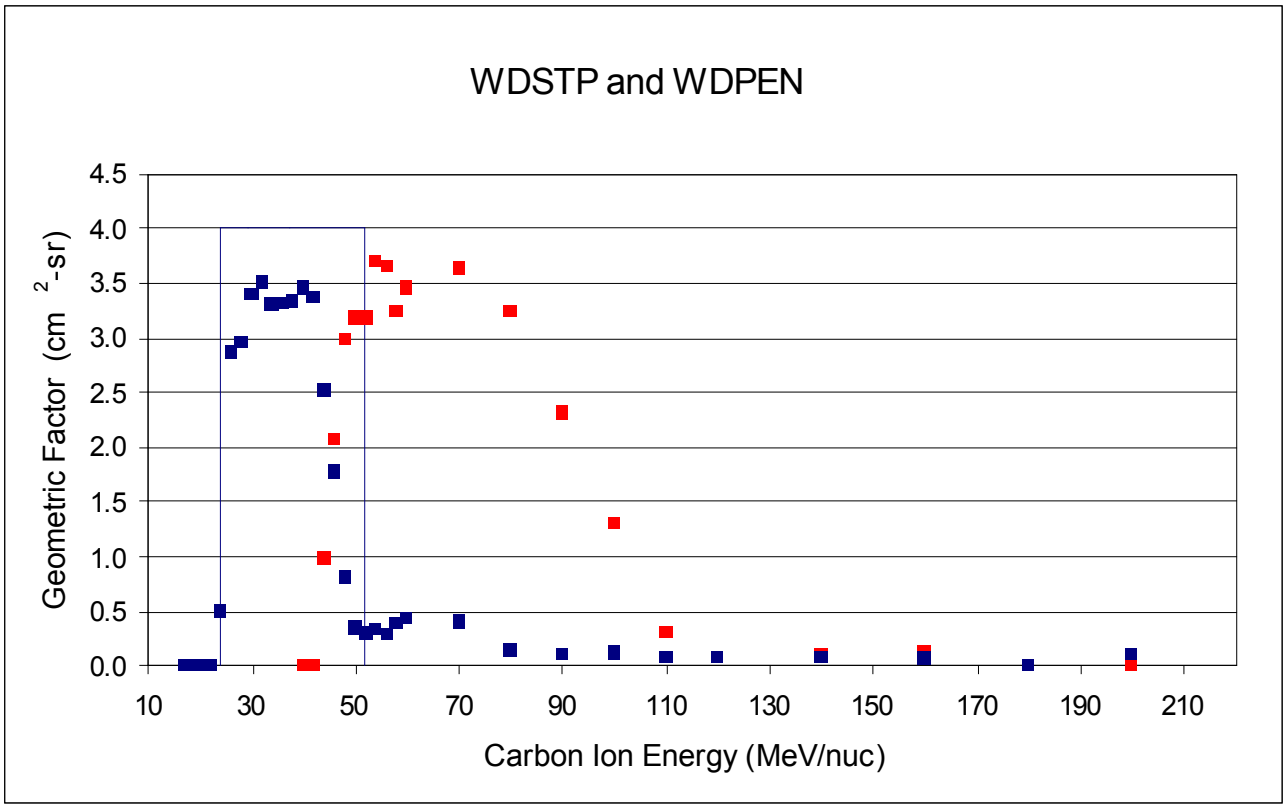

Fig. A14. LET E: Geant4 Result for WDSTP (Fig. A12) and WDPEN (Fig. A13) cases for the Carbon Ion (high energy cases). (blue squares = WDSTP and red squares = WDPEN)

OXYGEN ION

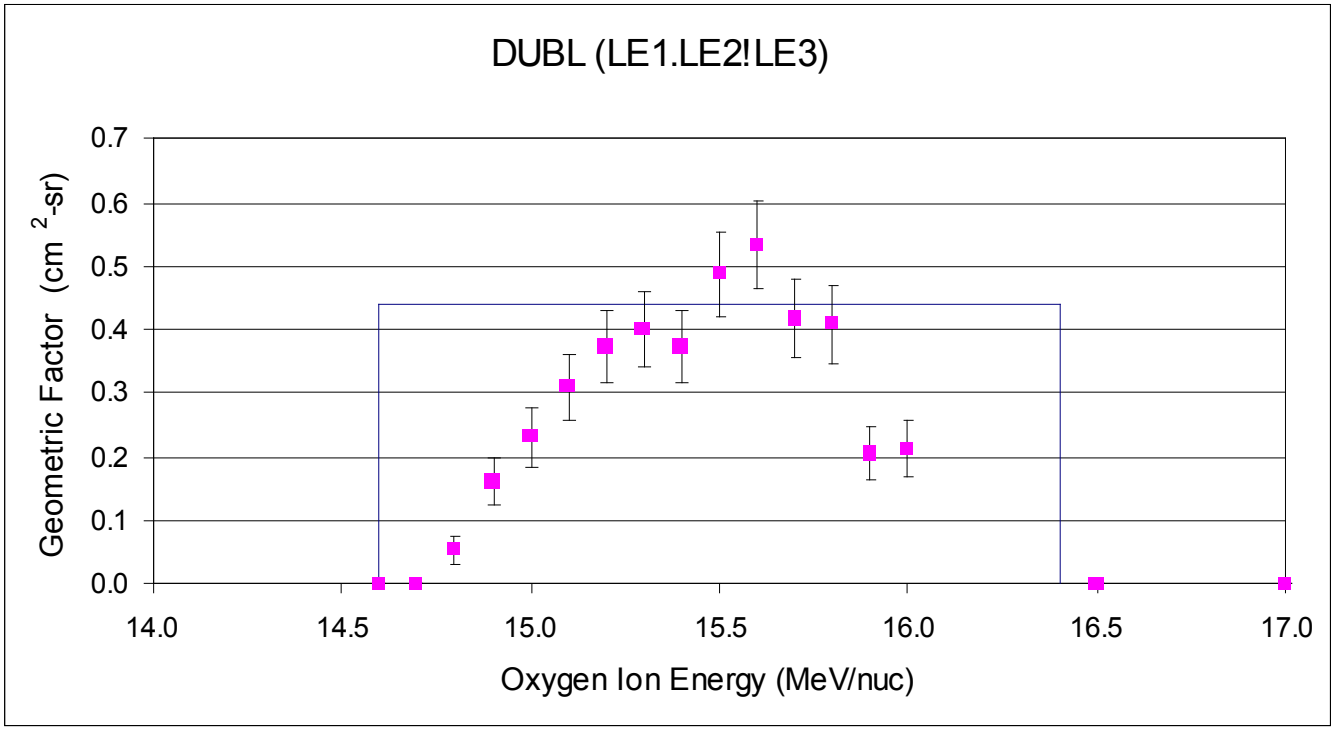

Fig. A15. LET E: Geant4 Simulation of Geometric Factor for the Oxygen Ion for the DUBL logic.

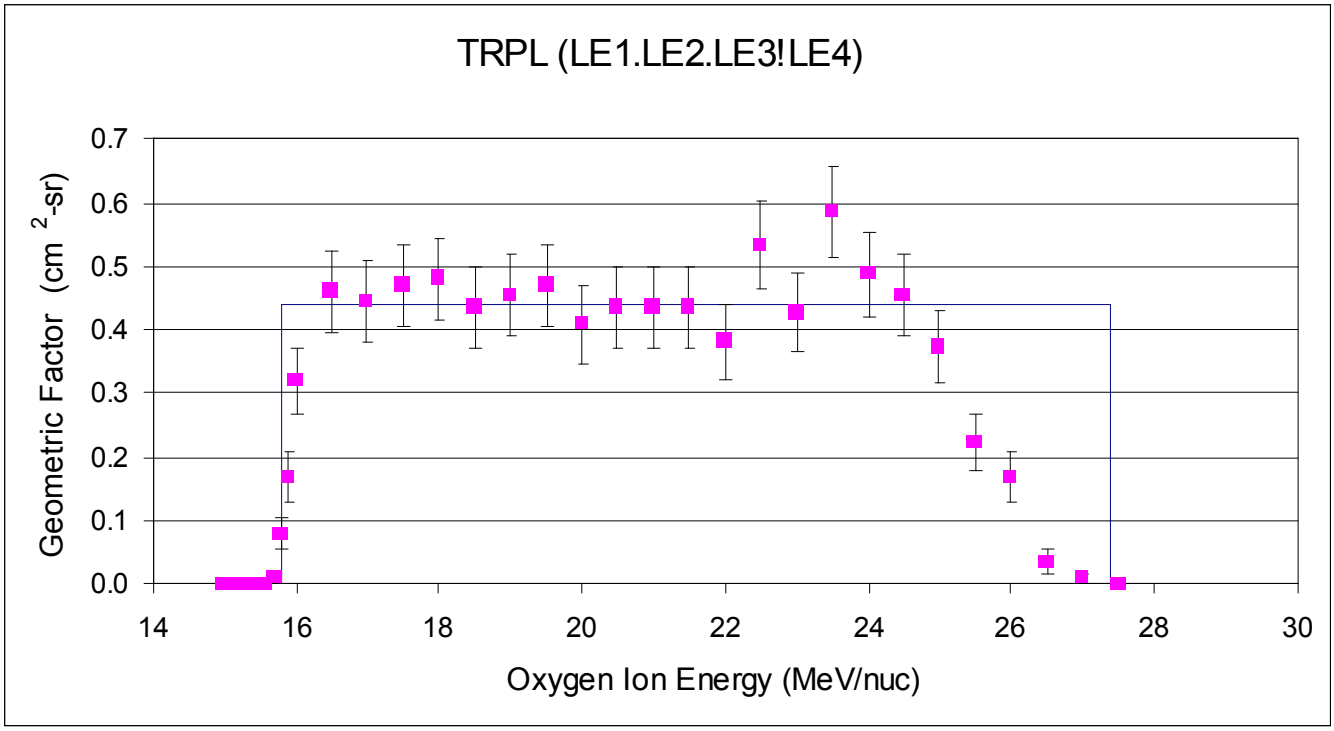

Fig. A16. LET E: Geant4 Simulation of Geometric Factor for the Oxygen Ion for the TRPL logic.

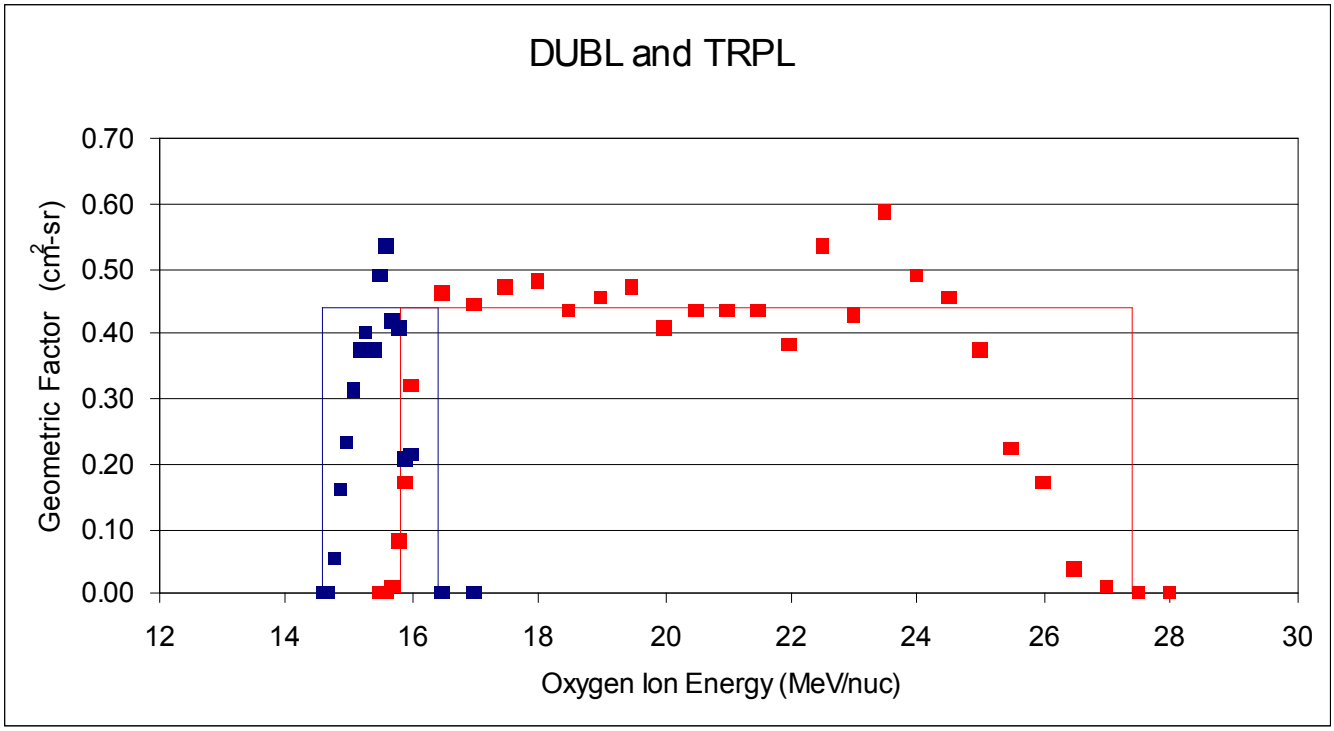

Fig. A17. LET E: G4 Simulation Result for DUBL (Fig. A15) and TRPL (Fig. A16) cases for the Oxygen Ion (low energy). (blue squares = DUBL and red squares = TRPL)

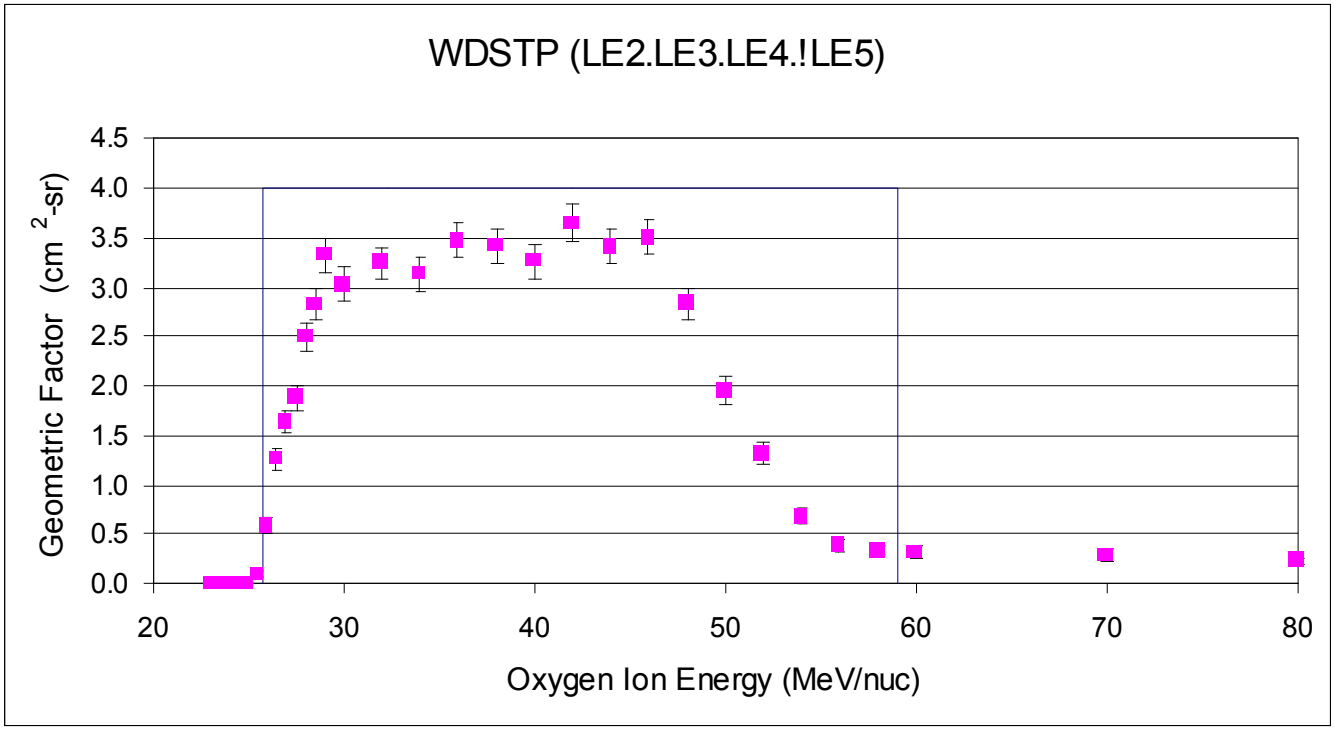

Fig. A18. LET E: Geant4 Simulation of Geometric Factor for the Oxygen Ion for the WDSTP logic.

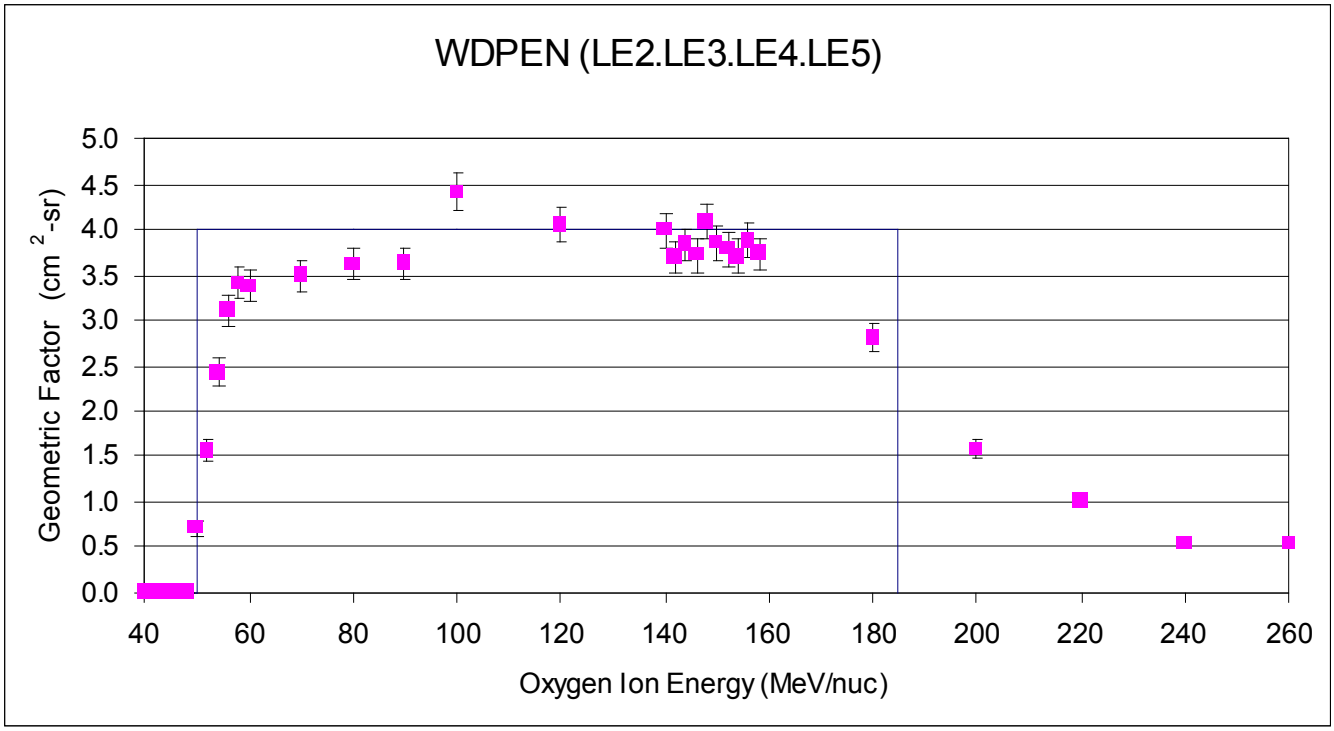

Fig. A19. LET E: Geant4 Simulation of Geometric Factor for the Oxygen Ion for the WDPEN logic.

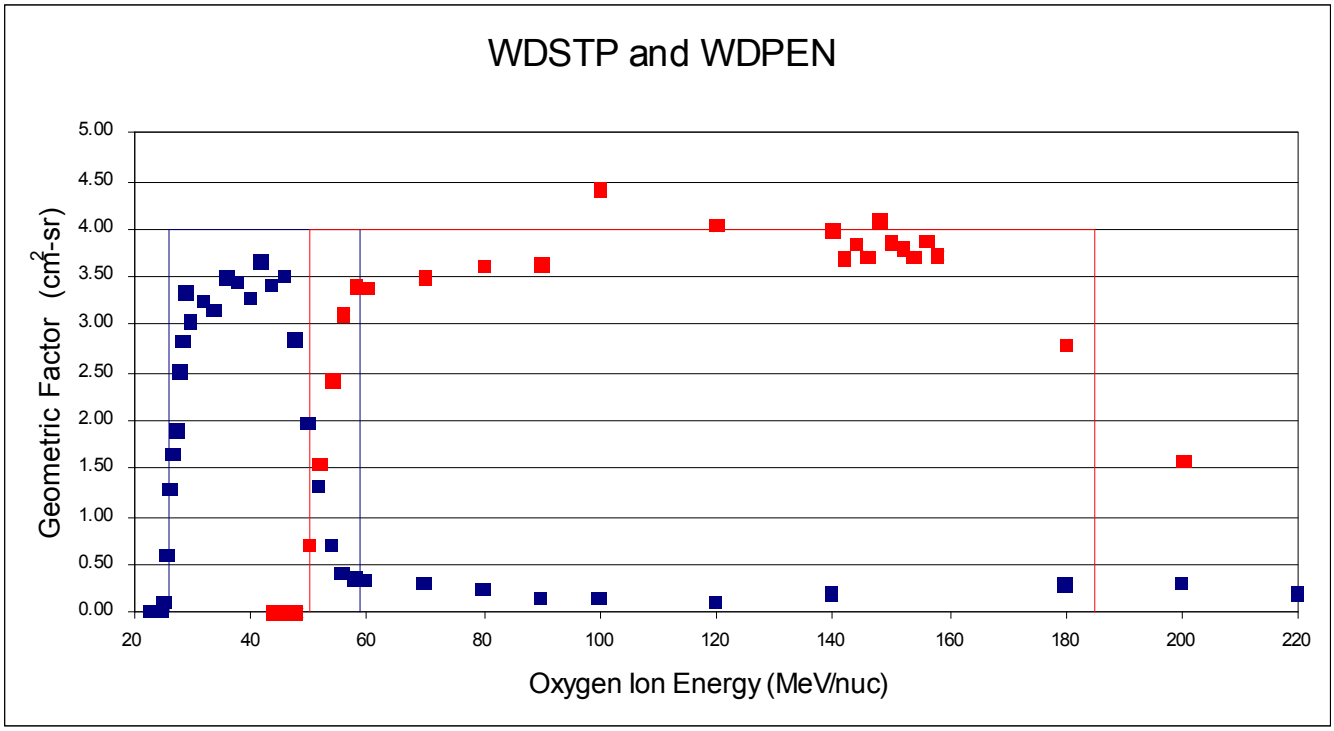

Fig. A20. LET E: G4 Simulation Result for WSTP (Fig. A18) and WDPEN (Fig. A19) cases for the Oxygen Ion (high energy cases) (blue squares = WDSTP and red squares = WDPEN)

SULFUR ION

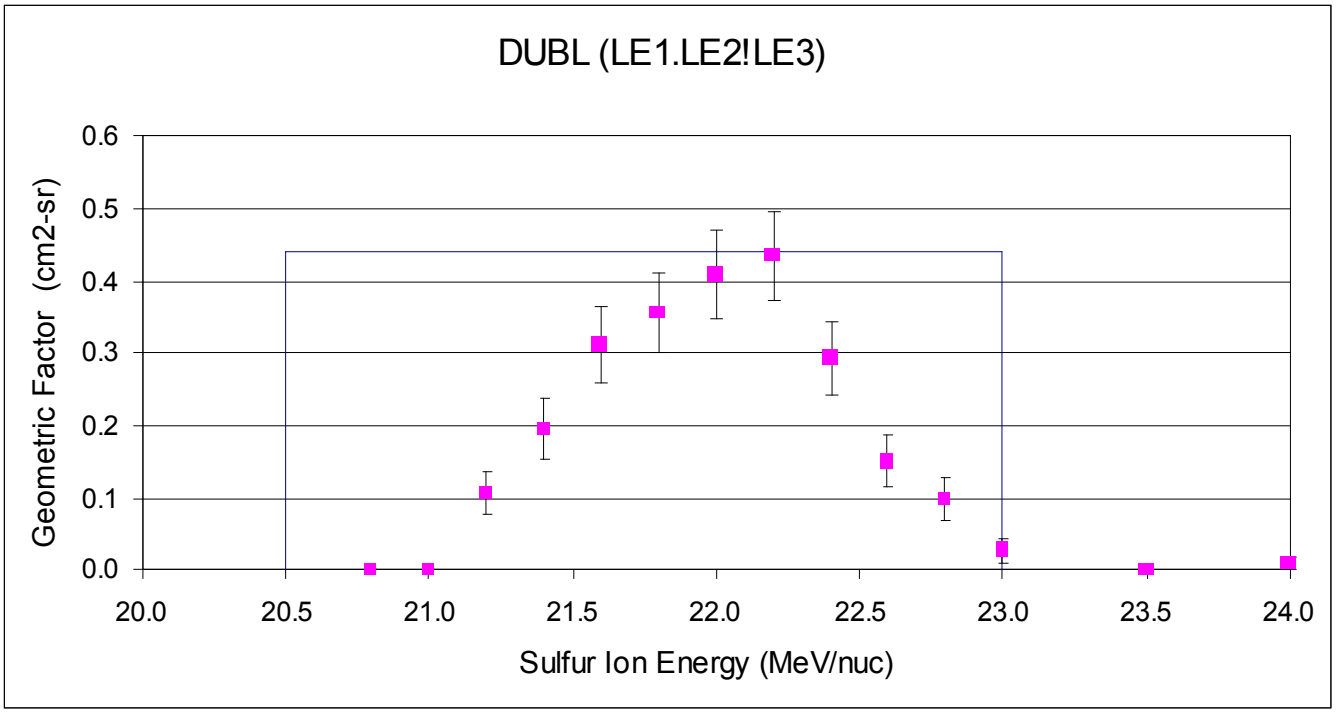

Fig. A21. LET E: Geant4 Simulation of Geometric Factor for the Sulfur Ion for the DUBL logic.

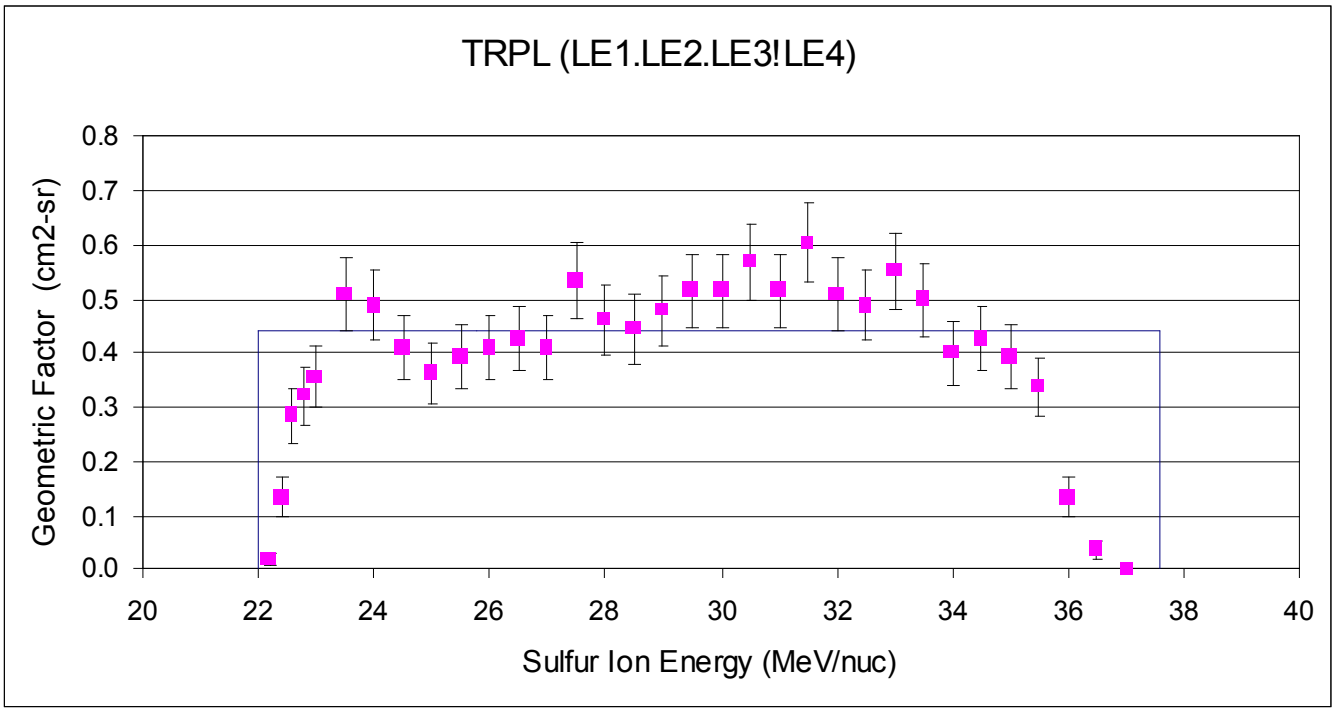

Fig. A22. LET E: Geant4 Simulation of Geometric Factor for the Sulfur Ion for the TRPL logic.

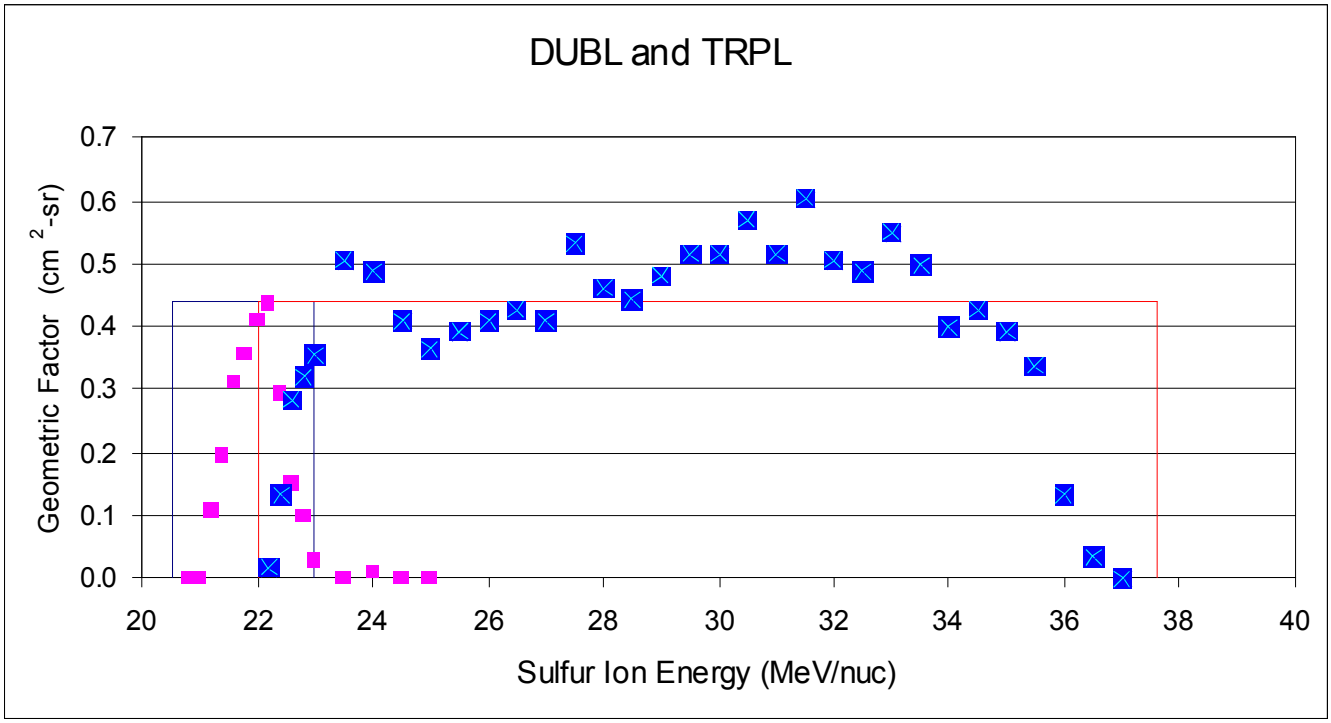

Fig. A23. LET E: G4 Simulation Result for DUBL (Fig. A21) and TRPL (Fig. A22) cases for the Sulfur Ion (low energy cases). (fuchsia squares = DUBL and blue squares = TRPL)

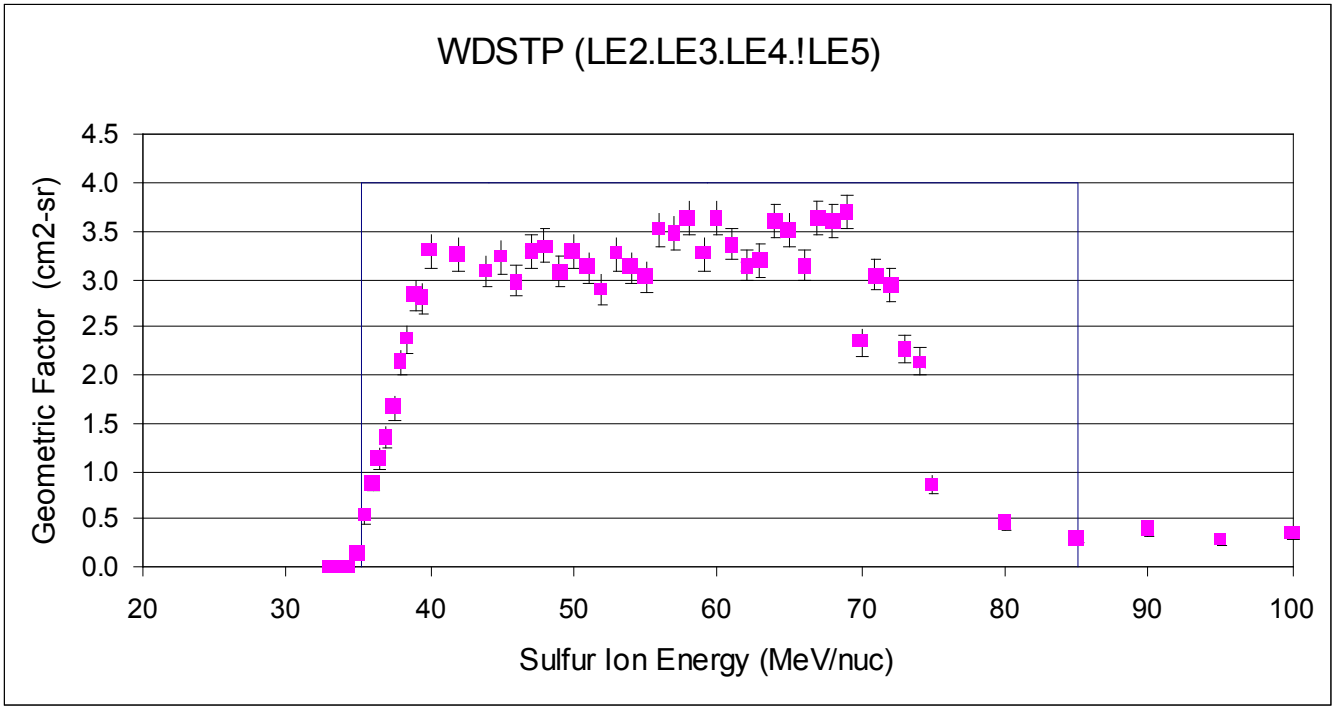

Fig. A24. LET E: Geant4 Simulation of Geometric Factor for the Sulfur Ion for the WDSTP logic.

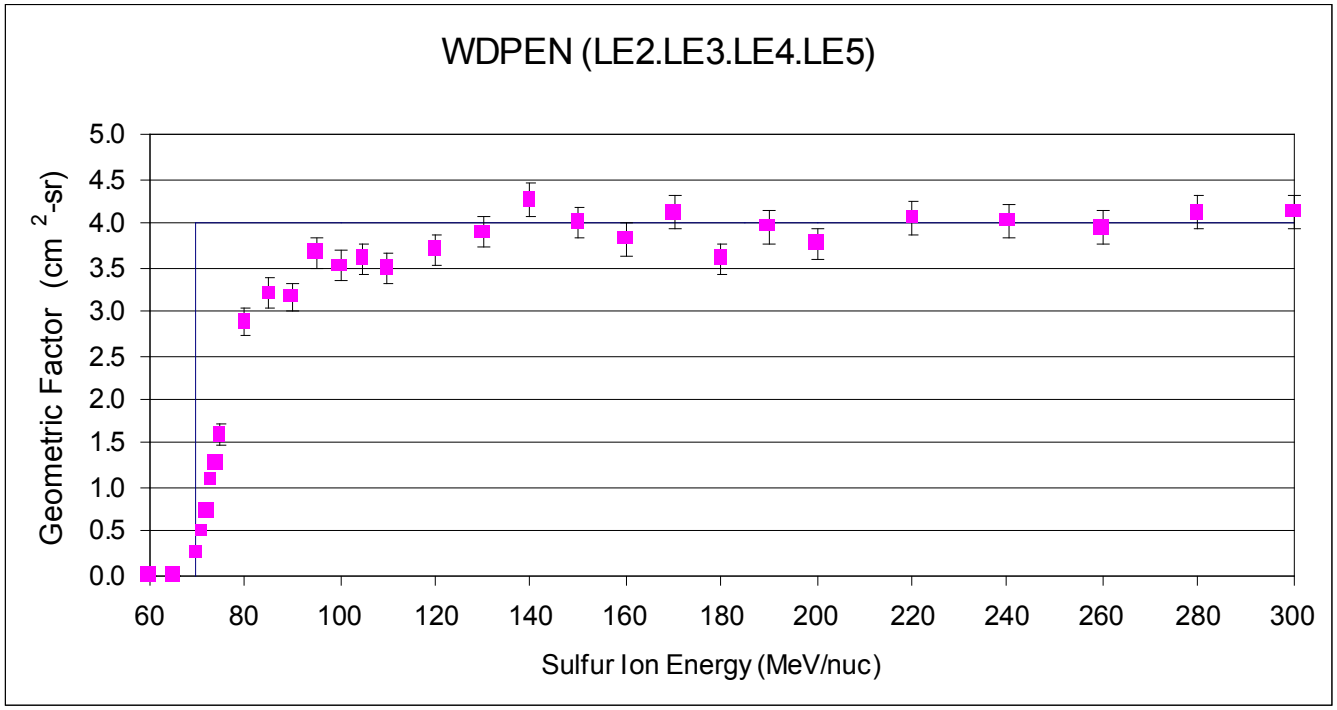

Fig. A25. LET E: Geant4 Simulation of Geometric Factor for the Sulfur Ion for the WDPEN logic

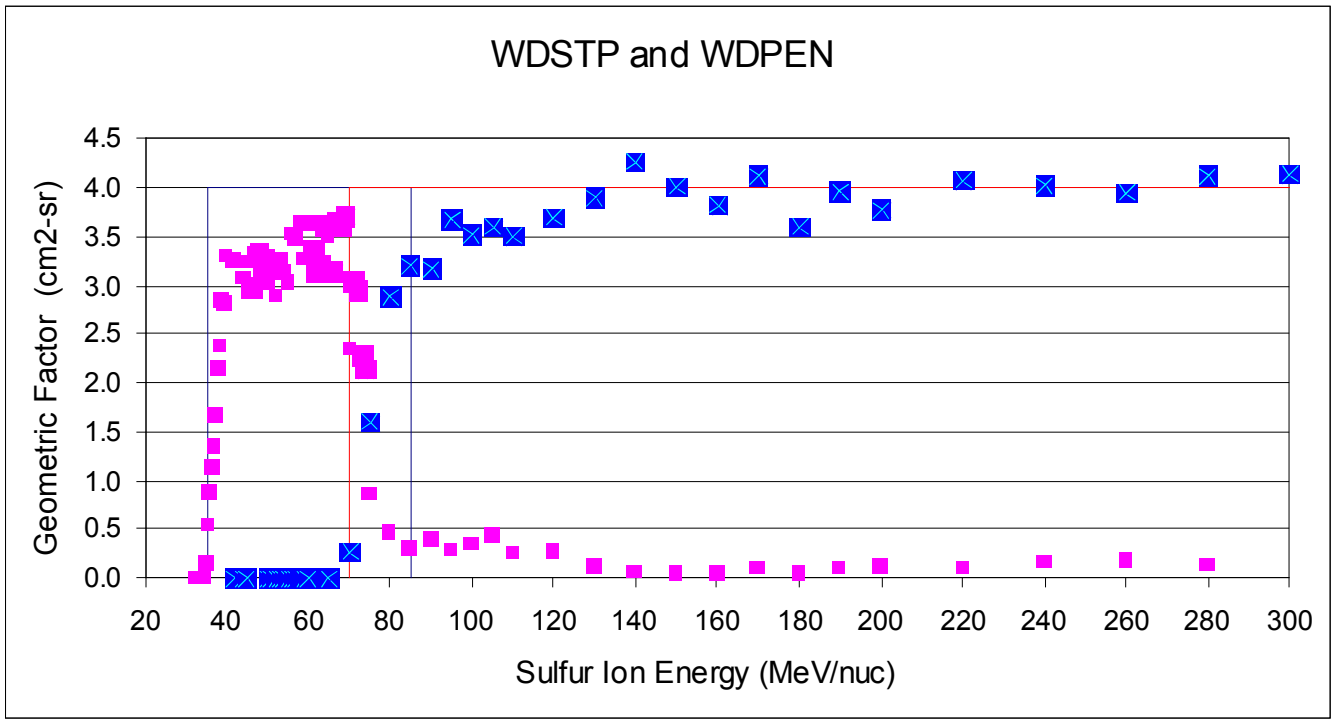

Fig. A26. LET E: G4 Simulation Result for WSTP (Fig. A24) and WDPEN (Fig. A25) cases for the Sulfur Ion (high energy cases). (fuchsia squares = WDSTP and blue squares = WDPEN)

APPENDIX IV REFERENCES

Anon., *LET B: Assembly Low Energy Det. Cosmic Ray Exp. MJS*, GD-1377938 D, Goddard Space Flight Center, Greenbelt, MD, 1991a.

Anon., *LET E: Assembly LET-E Ion Counter (HIC) Galileo*, GD-1406663, Goddard Space Flight Center, Greenbelt, MD, 1991b.

Agostinelli, S., J. Allison, K. Amak, J. Apostolakis, H. Araujo, et al., "Geant4 - a simulation toolkit", *Nuclear Instruments and Methods in Physics Research*, Section A, vol. 506, pp. 250–303, July 1, 2003. See also "Geant4", http://www.geant4.org/geant4/.

Garrard, T. L., N. Gehrels, and E. C. Stone, "The Galileo Heavy Element Monitor", *Space Sci. Rev.,* vol. 60, pp. 305–315, 1992. (Also available in SRL Publication 91-08).

Ziegler, J. F., "SRIM—The Stopping and Range of Ions in Matter", US Naval Academy, Annapolis, MD, http://www.srim.org/, 2011.

APPENDIX V. Acronyms and Abbreviations

CPU	Central Processor Unit
CRS	(Voyager) Cosmic Ray System
EPD	(Galileo) Energetic Particle Detector
GCR	Galactic Cosmic Rays
GPS	general particle source (Geant4)
GSFC	Goddard Space Flight Center
HIC	Heavy Ion Counter Experiment
JOI	Jupiter Orbit Insertion
LEMMS	Low-Energy Magnetospheric Measurement System
LET	Linear energy transfer
LET	low-energy telescope
LET B	low-energy telescope optimized for lower energy nuclei
LET E	high-energy telescope optimized for higher energy nuclei
NAIF	(NASA) Navigation and Ancillary Information Facility
PDS	Planetary Data System
PHA	pulse height analyzed (events)
R	radius
R_J	Jupiter radius, 71,400 km
SRIM	Stopping and Range of Ions in Matter code
TRIM	Transport of Ions in Matter code
UT	Universal Time
UTT	Unique Time Tag
Z	number of protons in the nucleus